Universidade de Aveiro Departamento de Electrónica, Telecomunicações e Informática,
2018

Manuel José Oliveira
São Bento Pereira

Compressão de Imagem utilizando Circuitos Óticos Integrados

Image Compression using Photonic Integrated Circuits

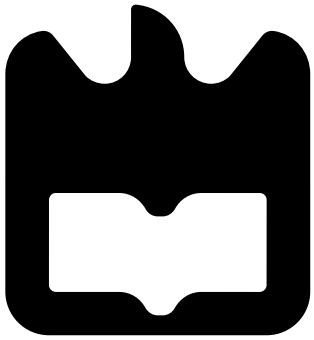

Manuel José Oliveira São Bento Pereira

Compressão de Imagem utilizando Circuitos Óticos Integrados
Image Compression using Photonic Integrated Circuits

Dissertação apresentada à Universidade de Aveiro para cumprimento dos requisitos necessários à obtenção do grau de Mestre em Engenharia Eletrónica e de Telecomunicações, realizada sob a orientação científica do Professor Mário Lima e do Professor António Teixeira, do Departamento de Eletrónica, Telecomunicações e Informática da Universidade de Aveiro.

Dissertation presented to the University of Aveiro for the fulfilment of the requisites necessary to obtain the degree of Master in Electronics and Telecommunications Engineering, developed under the scientific guidance of Professor Mário Lima and Professor António Teixeira, in the Department of Electronics, Telecommunications and Informatics of the University of Aveiro

O júri / The jury

presidente / president

Professor Doutor Paulo Miguel Nepomuceno Pereira Monteiro
Professor Associado no Departamento de Eletrónica, Telecomunicações e Informática da Universidade de Aveiro

vogais / examiners committee

Professor Doutor Mário José Neves de Lima
Professor Auxiliar no Departamento de Eletrónica, Telecomunicações e Informática da Universidade de Aveiro (orientador)

Professor Doutor Orlando José dos Reis Frazão
Professor Auxiliar na Faculdade de Ciências da Universidade do Porto (arguente)

Agradecimentos

Começar pelo mais importante: um obrigado especial aos meus pais por me permitirem passar 6 anos a completar este curso, sem nunca deixarem de oferecer todo o tipo de apoio. Hugo, Nuno, Mali e Ana, obrigado também a vocês por toda a vossa ajuda e pelas parvoíces que me foram aliviando alguns dias mais pesados.

Obrigado ao professor Mário Lima por toda a orientação exemplar e por toda a compreensão que mostrou ao longo do ano com situações particulares que apenas se tornaram mais toleráveis devido à sua ajuda.

Obrigado a todos os que me ajudaram com o desenvolvimento desta tese, em especial à Rita e à Cátia por todos os mails esclarecedores e ao Ricardo pelo array de fibras. Obrigado também ao meu amigo Jesus pela ajuda na fase final da tese.

Por fim, um obrigado a todos os meus amigos e colegas que me acompanharam durante este meu percurso académico, pois todos marcaram a minha vida, de uma forma ou de outra. Sendo impossível mencionar-vos a todos, deixo apenas um agradecimento especial ao trio que sempre se mostrou presente: Jesus, Cristiano e Jekas. A ti, Patrícia, devo-te tudo. Obrigado por me aturares este tempo todo e pelo apoio incondicional que sempre me ofereceste.

A preparação dos filmes baseados em di-ureasil foram preparados no âmbito da tese de PhD da Mestre Ana Rita, no laboratório CICECO - Instituto de Materiais de Aveiro. A Mestre Ana Rita realizou, também, as medidas experimentais de elipsometria espectroscópica e a sua modelação, com vista à qualificação do índice de refração em função da exposição à radiação UV. A adaptação do sistema de gravação por escrita direta foi realizada pela Mestre Ana Rita e pelo Doutor Carlos Vicente.

Este trabalho é financiado pela FCT/MEC através de fundos nacionais e quando aplicável cofinanciado pelo FEDER, no âmbito do Acordo de Parceria PT2020 no âmbito do projeto, COMPRESS - PTDC/EEI-TEL/7163/2014. O laboratório associado CICECO - Instituto de Materiais de Aveiro, POCI-01-0145-FEDER-007679 (FCT Ref. UID/CTM/50011/2013).

Resumo

A área das telecomunicações continua a evoluir e, dentro do ramo da ótica, os Circuitos Fotónicos Integrados são peças-chave para melhorar qualquer sistema. No projeto FCT COMPRESS, a Transformada de Haar, os Interferómetros Multimodo e o Magic-T são explorados e colocados em circuitos com o objetivo de processar e comprimir todos os tipos de sinais.

Estes circuitos são impressos através de um processo fotolitográfico, utilizando um laser pulsado ultra-violeta. Os circuitos são testados e os seus resultados analizados por uma aproximação Gaussiana. O seu sucesso é um passo certo em direção à implementação de novos circuitos com uma maior economização de energia e com uma maior capacidade de processamento.

Abstract

The telecommunications field keeps evolving, and inside the optics area, Photonic Integrated Circuits are crucial elements to improve any system's performance. In the FCT COMPRESS project, the Haar Wavelet Transform, the Multimode Interferometer, and the Magic-T are put together into circuits meant to process and compress any type of signals. These circuits are printed through a photolithography process, using an ultra-violet pulsed laser. The two-input circuits are tested and its results analyzed through a Gaussian approximation. Their success is a step closer to achieve circuits with a significant energy saving performance and a better processing capacity.

Contents

List of Figures

List of Tables

Acronyms

1D One-Dimensional.

2D Two-Dimensional.

3D Three-Dimensional.

CCD Charged-Coupled Detector.

CMT Coupled Mode Theory.

DCT Discrete Cosine Transform.

DFT Discrete Fourier Transform.

DWT Discrete Wavelet Transform.

FT Fourier Transform.

FWHM Full Width at Half Maximum.

GI General Interference.

HP High-Pass.

HT Haar Transform.

HWT Haar Wavelet Transform.

LP Low-Pass.

MM Multimode.

MMI Multimode Interference.

MPA Modal Propagation Analysis.

PI Paired Interference.

PIC Photonic Integrated Circuit.

RI Restricted Interference.

SI Symmetric Interference.

SSMF Standard Single-Mode Fiber.

TLS Tunable Laser Source.

UV Ultra-Violet.

WF Wavelet Function.

WT Wavelet Transform.

Chapter 1

Introduction

1.1 Context and Motivations

Technology belongs to our daily basis, and it keeps evolving at a breakneck pace. In the field of telecommunications, specifically in the optics area, Photonic Integrated Circuits (PICs) are the key to achieve a successful system. PICs are known for its compact size, low cost, low power consumption and ease of fabrication, which are significant characteristics to accomplish a good performance.

This thesis has three major concepts/components that need to be understood: the Haar Wavelet Transform (HWT), the Multimode Interference (MMI) mechanisms, and the Magic-T. These three elements are the essence of the FCT COMPRESS project (PTDC/EEITEL/7163/2014), which primary purpose is to implement layers of optical compression through these elements.

The HWT is an example of a Discrete Wavelet Transform (DWT), which means that its forward and inverse transforms only require additions and subtractions [1]. Considering all the types of DWTs, the HWT is the easiest to understand, and it has fast computation. The Magic-T is a 3-dB asymmetric coupler which performs additions and subtractions in the optical domain. Therefore, it allows the implementation of the HWT [2].

A MMI device is a N inputs x M outputs device that follows the self-imaging principle, and it is based on constructive and destructive interference mechanisms. In comparison with regular couplers, they have better performance due to the ease of fabrication and the compact size [3].

This dissertation intends to perform optical testing in circuits based on the previously mentioned vital elements. These circuits are printed through a process called photolithography, which uses the radiation of an Ultra-Violet (UV) pulsed laser to pattern the circuits

into a di-ureasil (organic-inorganic hybrid) substrate [4][5][6].

The two-input circuits are tested, and its results are examined through a Gaussian approximation. If the tests are successful, the advantages that can come from image compression are vast, such as more energy saving and better capacity processing performance.

1.2 Objectives

The primary goals of this thesis can be achieved by efficiently executing the following steps:

- Learn how the HWT operates and understand its network implementation;
- Study the MMI mechanisms and how it relates to the HWT and the Magic-T;
- Print the previously designed circuits in the scope of the FCT COMPRESS project through a photolithography process;
- Conduct a microscopic visual inspection of the resulting samples;
- Test the validated circuits of the best sample and interpret the results.

1.3 Structure Overview

This dissertation is structured as listed below:

- **Chapter 2: Haar Transform.** The Two-Dimensional (2D) theoretical implementation is examined, as well as an optical network implementation employing a Magic-T. A Haar Transform (HT) 3-dB asymmetric coupler design is also analyzed;
- **Chapter 3: Multimode Interference.** The self-imaging principle and the MMI component's structure is described. A detailed full-modal propagation breakdown of the MMI mechanisms is performed, as well as a thorough observation of its interference types;
- **Chapter 4: Printing Process.** The laboratory procedure concerning the printing of the previously designed circuits using an UV pulsed laser is demonstrated, and the resulting samples are visually inspected through a microscope;

- **Chapter 5: Circuits Characterization.** The experimental setup is displayed, and the testing technique is explained step-by-step for single and multiple-input circuits. The two-input circuits data is retrieved from the software, and a Gaussian approximation is applied. Final results are discussed;
- **Chapter 6: Conclusions and Future Work.** An overview of the work accomplished in this thesis and its conclusions. Some ideas for future research inside this project are also addressed.

1.4 Contributions

This thesis has some contributions, such as:

- Four printed samples with circuits intended for image processing and compression;
- Testing performance of the two-input circuits.

Chapter 2

Haar Transform

2.1 Introduction

Data compression is a critical operation in the area of real-time 2D data processing analysis, being a powerful tool for high definition image applications and redundant data reduction [7]. Digitally, an image can be interpreted as a group of pixels, where the neighboring pixels connect to each other, consequently becoming irrelevant in the overall image and occupying unnecessary space [8]. Therefore, the purpose of image compression is to reduce that redundancy by applying classic techniques based on fundamental sinusoidal functions such as Discrete Fourier Transform (DFT), Discrete Cosine Transform (DCT), DWT and more. All of these functions are orthogonal, which means that their forward and inverse transforms only require additions and subtractions. These provide an easy and efficient method of implementation on the computer [1].

The Wavelet Transform (WT) and the Fourier Transform (FT) are commonly used, and they are profitable tools. Nowadays, the DWT has been the most relevant since the WT surpasses the main limitation of the FT when it comes to representing non-stationary signals [9]. Wavelets are localized waves which do not endlessly oscillate like other transforms. Alternatively, they drop to zero, producing a natural multi-resolution (scaling) of every image, including all the significant edges (details) [8]. Hence, WT can perform the local spectral decomposition (Figure 2.1), which allows the dissection of a signal at various scales or resolutions [10].

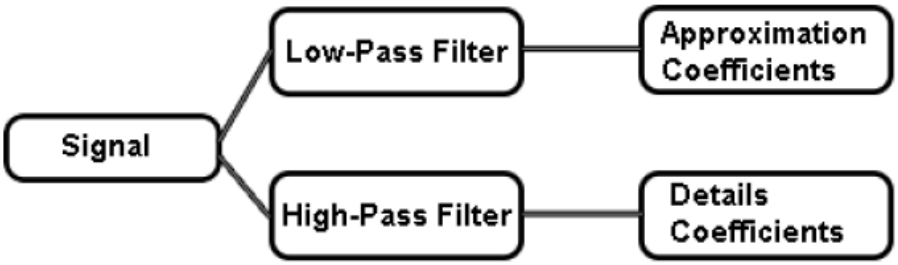

Figure 2.1: Multi-resolution analysis: signal decomposition [11]

Among the numerous representations of the WT, the HWT (also known as Daubechies D2 Wavelet) is the simplest one. It presents an effortlessly understandable design, fast computation and it can be implemented by optical planar interferometry, proving it to be a highly efficient compression technique and an example of multi-resolution analysis [2].

2.2 2D Theoretical Implementation

To simplify references, the research of the remaining sections of this chapter is essentially based on Parca, Teixeira, and Teixeira [2].

Generally, the DWT begins at the lowest scale/level (i.e., the original image) and estimates its coefficients by repeating the filtering and sub-sampling processes. It can render an image as a sum of Wavelet Functions (WFs), by distributing the signal into sets of detail and approximation coefficients [8].

Since the HWT is a model of a DWT, orthogonality is a recognized characteristic, making it conceivable to capture both Low-Pass (LP) and High-Pass (HP) behaviors of an image and to filter it, dismissing duplicated information. A system building blocks for an all-optical 2D implementation of the HWT is presented below:

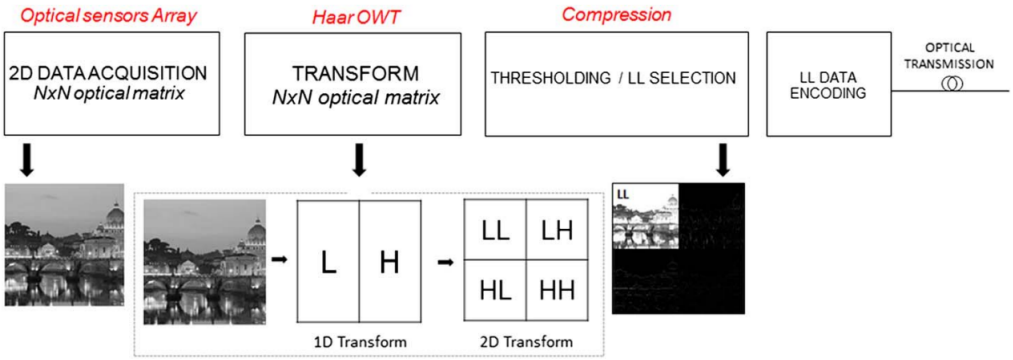

Figure 2.2: System building blocks for an all-optical implementation of HWT [2]

By observing Figure 2.2, the system can be broken into four main stages regarding data treatment, plus transmission: Acquisition, Transform, Compression and Encoding. In the first stage, data is collected through light detection using optical sensors, and then it goes through sampling, originating a N x N optical input data matrix.

Subsequently, it moves into the Transform block, where the HWT is employed. This step incorporates LP and HP filters correlated with the HWT. These are only applied over one dimension at once. The LP supplies the approximation coefficients while the HP gets the horizontal, vertical and diagonal details. This filtering process can be defined as the calculations of the average between two adjacent pixels (LP) or the difference between them (HP).

The HWT scattering matrix is displayed in Figure 2.3, and it generates at its output the average and the difference of the input signal.

$$S = \begin{bmatrix} \frac{1}{\sqrt{2}} & \frac{1}{\sqrt{2}} \\ \frac{1}{\sqrt{2}} & -\frac{1}{\sqrt{2}} \end{bmatrix}$$

Figure 2.3: HWT Matrix [2]

$$\begin{bmatrix} \vdots \\ c_{10} \\ d_{10} \\ c_{11} \\ d_{11} \\ c_{12} \\ d_{12} \\ \vdots \end{bmatrix} = \frac{1}{\sqrt{2}} \begin{bmatrix} \cdots & & & \cdots & & & \cdots \\ & 1 & 1 & 0 & 0 & 0 & 0 & \\ & 1 & -1 & 0 & 0 & 0 & 0 & \\ & 0 & 0 & 1 & 1 & 0 & 0 & \\ \vdots & & & & & & & \vdots \\ & 0 & 0 & 1 & -1 & 0 & 0 & \\ & 0 & 0 & 0 & 0 & 1 & 1 & \\ & 0 & 0 & 0 & 0 & 1 & -1 & \\ \cdots & & & \cdots & & & \cdots \end{bmatrix} \begin{bmatrix} \vdots \\ a_0 \\ a_1 \\ a_2 \\ a_3 \\ a_4 \\ a_5 \\ \vdots \end{bmatrix}$$

Figure 2.4: N x N input data matrix for One-Dimensional (1D) HWT [2]

In Figure 2.4, it is contemplated a N x N input data matrix (previously sampled), the corresponding 1D HWT matrix (a_i coefficients) and the resulting scaling c_{ij} and detail d_{ij} coefficients (i: transform level; j: coefficients index), gathered from the LP and HP filtering, respectively, of each pixel pair.

Therefore, the decomposition of four sub-bands (LL, LH, HL, HH) is attained (Figure 2.5) and it matches the first level transform.

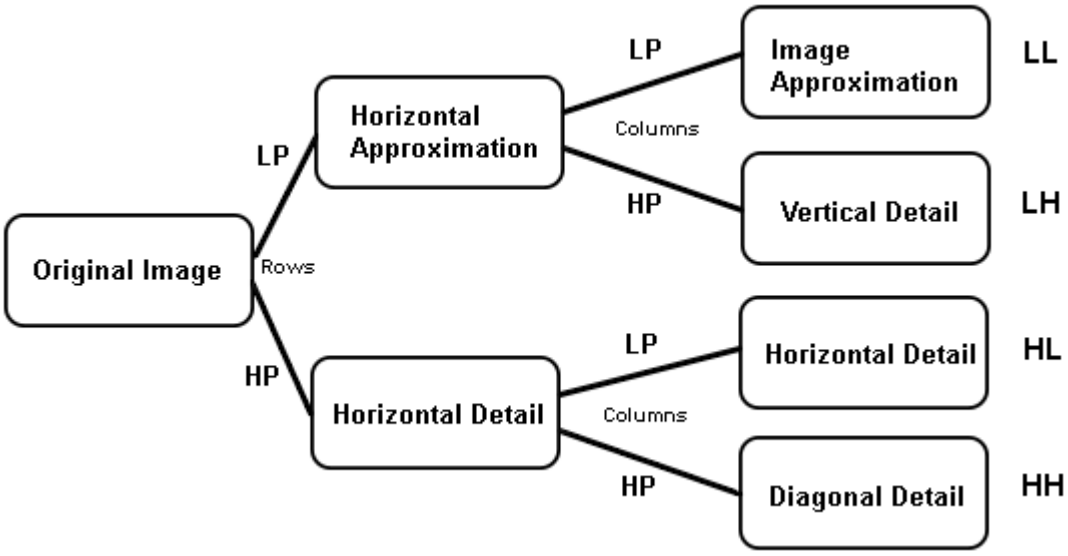

Figure 2.5: Band decomposition of an image using HWT [11]

Regarding a 2D N x N input data matrix, this method must be executed twice, horizontally then vertically, for each transform level, so the intensity fluctuations across the image can be assessed along the two dimensions. To reach higher transform levels, the same filtering operation must be applied just to the LL sub-band. The other sub-bands are either stored, transmitted or rejected since the transform coefficients are associated with high-frequency components.

Next, the Compression block manages quantization and selection, while the sharp reduction is implemented and specific elements within the coefficients set are extracted. The last block (Encoding) is responsible for compressed data encoding, bitstream production and adaptation to the optical channel, where the data is finally transmitted.

If the retrievement of information is required, a symmetric system can perform the inverse process: decoding, dequantization and inverse transformation.

2.3 Optical Network Implementation using a Magic-T

3-dB asymmetric couplers are also known as Magic-T [12], and they can implement the HT since their scattering matrix (same as in Figure 2.3) perfectly replicates the required average and difference between each optical input pair, as seen in Figure 2.6.

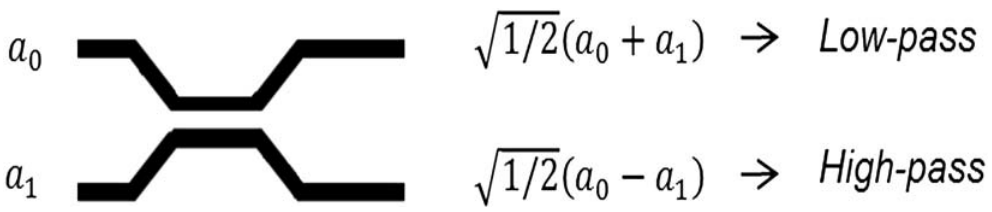

Figure 2.6: Magic-T scheme [2]

To probe 2D data, a Three-Dimensional (3D) basic module (Figure 2.7), based on a Magic-T network, can accomplish low and high filtering on one dimension a time, through the scattering matrix mentioned previously.

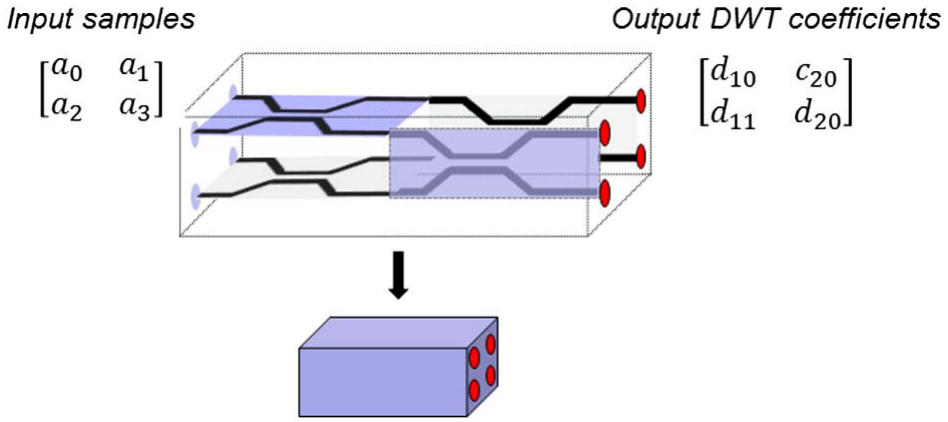

Figure 2.7: 3D basic module for first-level optical 2D HT [2]

Observing the previous figure, the original image corresponds to a 2 x 2 input matrix. The first LP-HP filtering step befalls along only one dimension (horizontal), exhibiting four intermediary outputs. These go through another LP-HP filtering stage, this time along the vertical dimension, producing the scaling c_{ij} and detail d_{ij} coefficients (i: filtering step on each dimension; j: coefficients index), creating the first-level HWT. This module can be scaled by extending the number of inputs and by arranging them in cascade, consequently developing a N x N 3D integrated passive scheme for all-optical HWT (Figure 2.8)

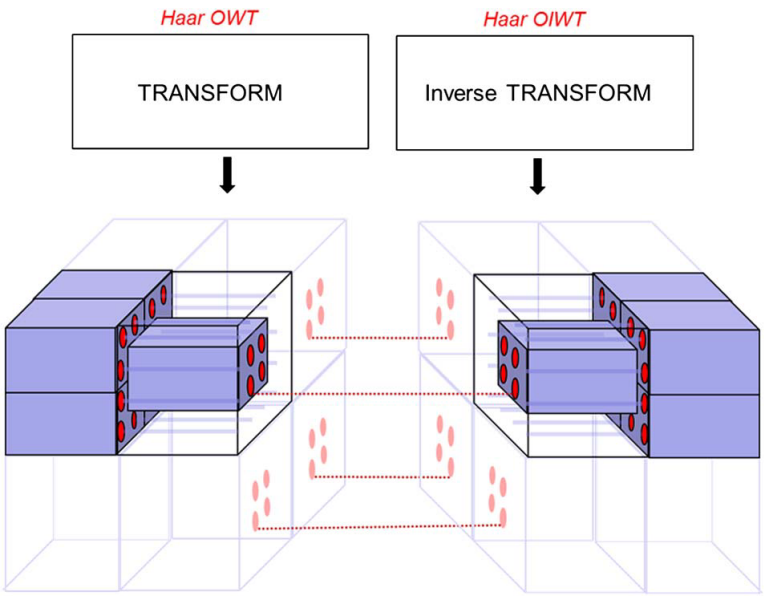

Figure 2.8: Integrated passive scheme for all-optical HWT [2]

Unfortunately, this project is considered for lossy compression techniques due to a portion of the data being discarded, so the inverse transform could receive less information. Notwithstanding, since the human eye is less sensitive to high-frequency components and more sensitive to low-frequency signals, this compression method can be approximated to lossless by giving more importance to the latter sub-bands, which means applying a precise reduction or thresholding on the first ones.

2.4 Haar Transform 3-dB Asymmetric Coupler Design

A 3-dB asymmetric coupler design, simulation and optimization were previously considered in [2, 8]. It is based on the Coupled Mode Theory (CMT), which states that if optical power is being pushed at a waveguide from an array of coupled waveguides, then that power is transferred between the guided modes from each waveguide of the array [11].

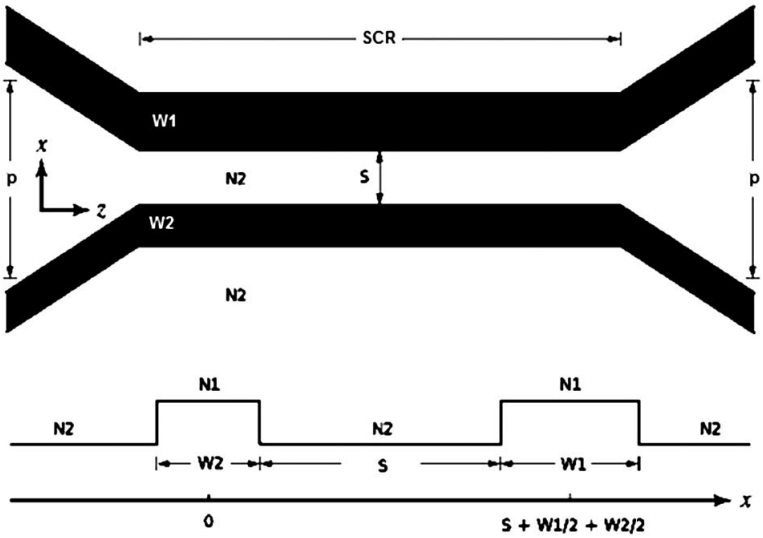

Figure 2.9: 3-dB asymmetric coupler scheme [2]

The output values of power and phase were simulated to satisfy the π@3dB condition, which has the following requirements:

- two nonidentical waveguides must have a maximum coupling of 50%;
- the output signals need to be in phase (sum) with the input injected into the wider waveguide (W1);
- when the input is injected into the narrowed waveguide (W2),
  - W2's output needs to have a 180° phase difference (subtraction) with the input;
  - W1's output must have a null phase shift, compared with the input.

The simulations results were obtained, and they achieved the condition's obligations, but the system can still be improved.

MMI devices are one viable solution since they also fulfill the π@3dB condition. When compared to couplers, they have many advantages, for instance, they are easily fabricated, and they also have a much smaller size. Regarding Multimode (MM) fibers, MMI devices are able to control better the higher number of modes.

Chapter 3

Multimode Interference

To not overwhelm this section with citations, most of this chapter is based on Soldano and Pennings [3], where an in-depth study on integrated optics routing and coupling devices based on MM interference is made.

3.1 Self-Imaging Principle

Nowadays, PICs must be adaptable, reconfigurable, broad in bandwidth and exceptionally compact, so that they can be produced at a much lower cost. MMI devices are being exponentially used in optical coupling and switching applications, due to their advantages of low loss, compactness and good fabrication tolerances. These properties allow MMI-based components to be integrated with other devices on a photonic chip [13].

A MMI device obeys the self-imaging principle which states: "self-imaging is a property of MM waveguides by which an input field profile is reproduced in single or multiple images at periodic intervals along the propagation direction of the guide". Essentially, waveguides can create periodic images of an object.

3.2 Structure

A MMI component's structure is arranged into two main sections: access waveguides and the central block, as it can be seen in Figure 3.1 The access waveguides (generally, these propagate single-mode) are responsible for sending (inputs) and retrieving (outputs) light from the central block, which is a MM waveguide that can propagate 3 or more modes. These components are designated as N x M MMI couplers (N: number of input waveguides; M: number of output waveguides).

Figure 3.1: N x M MMI coupler's structure [11]

3.3 Full-Modal Propagation Analysis

In this section, a Modal Propagation Analysis (MPA) of MMI's methods is performed since it is the best theoretical tool to comprehensibly describe the self-imaging principle.

3.3.1 Multimode Waveguide Constants

In Figure 3.2, it is shown a step-index MM waveguide of width W_M, ridge (effective) refractive index n_r and cladding (effective) refractive index n_c. This waveguide can propagate m lateral modes with numbers $v = 0, 1, ...(m-1)$, at a free-space wavelength λ_0, as it can be observed in Figure 3.3.

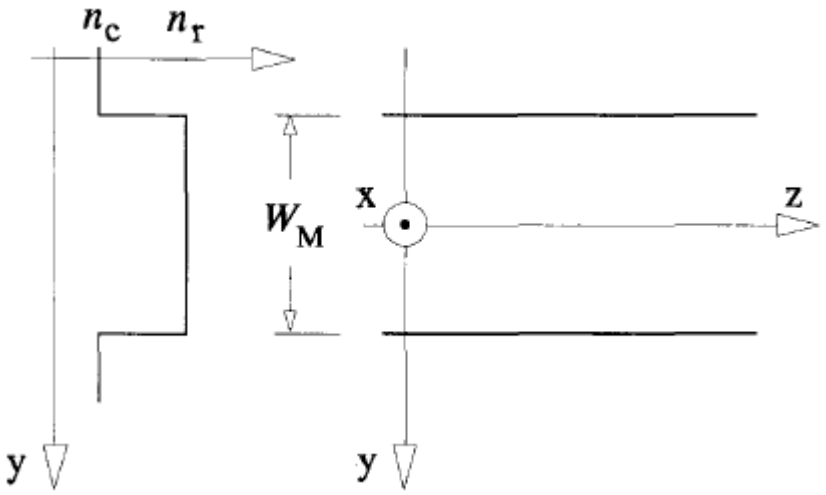

Figure 3.2: 2D representation of a step-index MM waveguide. Left: effective index lateral profile; Right: top view of ridge boundaries and coordinate system [3]

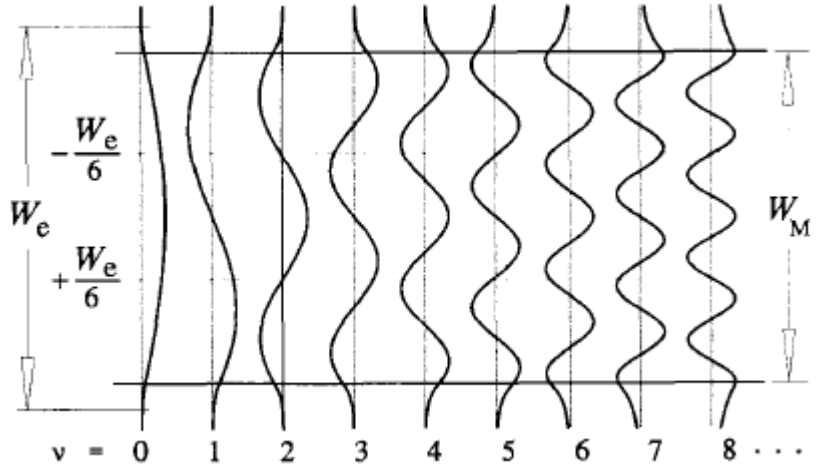

Figure 3.3: Example of the first 9 guided modes in a step-index MM waveguide [3]

The lateral wave-number k_{yv} (y: number of waveguide; v: number of mode) and the propagation constant β_v are related by the following equations:

$$k_{yv}^2 + \beta_v^2 = k_0^2 n_r^2, \tag{3.1}$$

with

$$k_0^2 = \frac{2\pi}{\lambda_0}, \tag{3.2}$$

$$k_{yv} = \frac{(v+1)\pi}{W_{ev}}. \tag{3.3}$$

W_{ev} is the "effective" width which is affected by the lateral penetration depth of each mode field but only for low-contrast waveguides since this depth is very small for the high-contrast ones, hence $W_{ev} \approx W_M$. Usually, W_{ev} is approximated by the width corresponding to the fundamental mode, $W_{e0} = W_e$. From equations 3.1 to 3.3, β_v is deducible:

$$\beta_v \approx k_0 n_r - \frac{(v+1)^2 \pi \lambda_0}{4 n_r W_e^2}. \tag{3.4}$$

Also, interpreting L_π as the beat length of the two lowest-order modes

$$L_\pi = \frac{\pi}{\beta_0 - \beta_1} \approx \frac{4 n_r W_e^2}{3\lambda_0}, \tag{3.5}$$

allows the propagation constants spacing to be written as

$$(\beta_0 - \beta_v) = \frac{v(v+2)\pi}{3L_\pi}. \tag{3.6}$$

3.3.2 Guided-Mode Analysis

A MPA is conducted to explain where the images are placed along the waveguide, as Figure 3.4 illustrates:

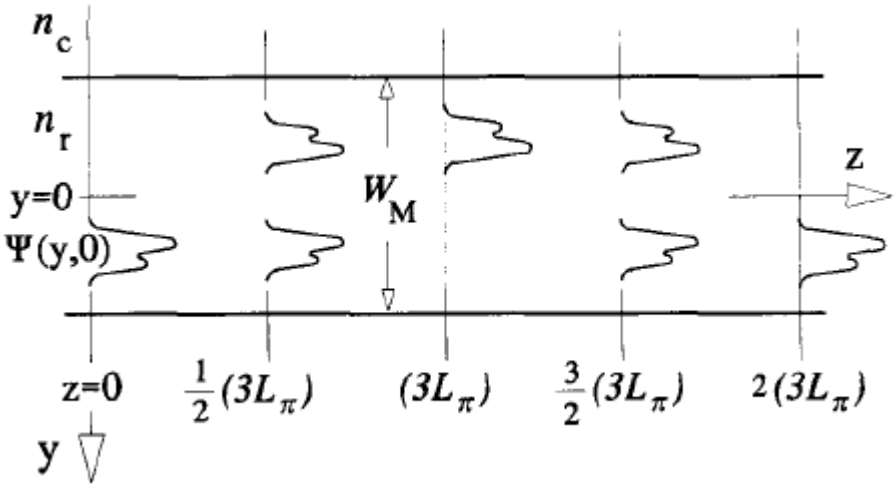

Figure 3.4: Input field and mirrored images along the MM waveguide [3]

The input field profile at a distance z can be defined as a superposition of all the guided mode field distributions ($\psi_v(y)$), where the field excitation coefficients are denoted by c_v:

$$\Psi(y,z) = \sum_{v=0}^{m-1} c_v \psi_v(y) e^{j(\omega t - \beta_v z)}. \tag{3.7}$$

Phase is a common factor to every mode, so the exponential part $(\omega t - \beta_v z) = (\beta_0 - \beta_v)z$, and assuming that the field is time-dependent, an expression for the field at $z = L$ can be written by mixing equations 3.6 and 3.7:

$$\Psi(y,L) = \sum_{v=0}^{m-1} c_v \psi_v(y) e^{j\frac{v(v+2)\pi}{3L_\pi}L}. \tag{3.8}$$

Observing this last equation, it is feasible to extract the mode phase factor (Equation 3.9) and the modal excitation c_v:

$$e^{j\frac{v(v+2)\pi}{3L_\pi}L}. \tag{3.9}$$

These will format the shape of $\Psi(y, L)$ and the kind of images formed, which can be divided in General Interference (GI) or Restricted Interference (RI).

3.4 General Interference

GI consists of the self-imaging mechanisms which are independent of the modal excitation. These examine the mode phase factor (Equation 3.9) and by analyzing Equation 3.8, it is a straightforward conclusion that a single image is reproduced ($\Psi(y, L) = \Psi(y, 0)$) if

$$e^{j\frac{v(v+2)\pi}{3L_\pi}L} = 1 \;\; or \;\; (-1)^v. \tag{3.10}$$

The first condition states that the shifts in phase of all the modes along L must differ by integer multiples of 2π, consequently producing a direct replica of the input field since all guided modes interfere with the same relative phases as in $z = 0$.

The second condition asserts that these phase variations must be alternatively odd and even multiples of π, being the first ones out-of-phase and the latter in-phase, hence arising a mirrored single image only on the odd modes. Clearly, the first and second conditions are accomplished at

$$L = p(3L_\pi) \;\; with \;\; p = 0, 1, 2... \tag{3.11}$$

for p even and p odd, respectively. The factor p manifests the periodic behavior of the self-imaging mechanisms throughout the MM waveguide.

Additionally to the single images, multiple ones are located along the waveguide. Regularly, these are found at intermediate z-positions but through a (spatial) Fourier expansion and adopting proprieties of the generalized Gaussian sums, an analytic expression for the distances between the n-fold images was obtained:

$$L = \frac{p}{N}(3L_\pi), \tag{3.12}$$

where $p \geq 0$ and $N \geq 1$ are integers with no common divisor other than 1. Therefore, the field is written as

$$\Psi(y, L) = \frac{1}{C} \sum_{q=0}^{N-1} \Psi_{in}(y - y_q) e^{j\varphi_q}, \tag{3.13}$$

with

$$y_q = p(2q - N)\frac{W_e}{N}, \tag{3.14}$$

$$\varphi_q = p(N - q)\frac{q\pi}{N}, \tag{3.15}$$

where C is a complex normalization constant where $|C| = \sqrt{N}$, p aims to the imaging periodicity throughout z and q consists of each of the N images along y. These equations prove that, at a distance $z = L$, N images are generated from the field $\Psi_{in}(y)$, positioned at y_q, each with amplitude $1/\sqrt{N}$ and phase φ_q. Identifying the images' positions and their relative phases at the output ports is very crucial in designing MMI devices.

The multiple self-imaging method confirms that the fabrication of N x N or N x M optical couplers is achievable and compact devices are attained for $p = 1$. For instance, the optical phases of a N x N MMI coupler are obtained by

$$\varphi_{rs} = \frac{\pi}{4N}(s - 1)(2N + r - s) + \pi, \quad for\ r + s\ even \tag{3.16}$$

$$\varphi_{rs} = \frac{\pi}{4N}(r + s - 1)(2N - r - s + 1), \quad for\ r + s\ odd \tag{3.17}$$

where $r = 1, 2, ...N$ and $s = 1, 2, ...N$ are the bottom-down and top-down numbering of the inputs and the outputs, respectively.

3.5 Restricted Interference

RI comprises the self-imaging mechanisms which are obtained by exciting solely specific modes, contrary to GI's modal excitation independence. RI supports the fabrication of more compact MMI devices, and it is classified within two varieties: Paired Interference (PI) and Symmetric Interference (SI). Table 3.1 shows a summary of each mechanism's characteristics:

Interference Mechanism	General	Paired	Symmetric
Inputs x Outputs	N x N	2 x N	1 x N
1st single-image distance	$3L_\pi$	L_π	$3L_\pi/4$
1st N-fold image distance	$3L_\pi/N$	L_π/N	$3L_\pi/(4N)$
Excitation Requirements	none	$c_v = 0\ for\ v = 2, 5, 8, ...$	$c_v = 0\ for\ v = 1, 3, 5, ...$
Input(s) Location(s)	any	$y = \pm W_e/6$	$y = 0$

Table 3.1: Characteristics of the Self-Imaging Mechanisms

3.5.1 Paired Interference

Considering that

$$mod_3[v(v+2)] = 0 \ \ for \ \ v \neq 2, 5, 8, ... \tag{3.18}$$

it is possible to lessen the length periodicity of the mode phase factor (Equation 3.9) by a factor of three if

$$c_v = 0 \ \ for \ \ v = 2, 5, 8, ... \tag{3.19}$$

Thus, single (direct and mirrored) and multiple image copies are respectively found through Equations 3.20 and 3.21:

$$L = p(L_\pi) \ \ with \ \ p = 0, 1, 2, ... \tag{3.20}$$

$$L = \frac{p}{N}(L_\pi) \tag{3.21}$$

where $p \geq 0$ and $N \geq 1$ are integers with no common divisor other than 1. Two-fold images are settled at $L = \frac{p}{2}L_\pi$ with p odd. Selective excitation is realized by launching an even symmetric input field at $y = \pm\frac{W_e}{6}$ since at this positions, the modes $v = 2, 5, 8...$ present a zero with odd symmetry, as illustrated in Figure 3.3.

When the condition stated in Equation 3.19 is succeeded, the contributing modes are matched and each even mode leads its odd partner by a phase difference of $\frac{\pi}{2}$ at the 3-dB length, $z = \frac{L_\pi}{2}$.

3.5.2 Symmetric Interference

N-way splitters are formed through GI's multiple imaging mechanism. Nevertheless, by exciting only the even symmetric modes, 1 x N beam splitters are created with a length periodicity four times shorter. Considering that

$$mod_4[v(v+2)] = 0 \;\; for \;\; v\, even, \tag{3.22}$$

the decrease in the above mentioned periodicity of the mode phase factor is unambiguous if

$$c_v = 0 \;\; for \;\; v = 1, 3, 5, ... \tag{3.23}$$

Accordingly, if the odd modes avoid the MM waveguide's excitation, single (Equation 3.24) and multiple (Equation 3.25) images of the input field $\Psi(y, 0)$ will be created. This imaging is captured by linear combinations of the even symmetric modes,

$$L = p(\frac{3L_\pi}{4}) \;\; with \;\; p = 0, 1, 2, ... \tag{3.24}$$

$$L = \frac{p}{N}(\frac{3L_\pi}{4}) \tag{3.25}$$

where $p \geq 0$ and $N \geq 1$ are integers with no common divisor other than 1, and the N images of the input field are symmetrically positioned along the y-axis with equal-spacing of $\frac{W_e}{N}$.

Chapter 4

Printing Process

4.1 Introduction

Lithography is a printing process that consists of the image zones being patterned onto a flat stone or metal plate, using a greasy substance, so that the ink will adhere to them, while the non-image areas are made ink-repellent. Photolithography is an example of this concept, where the radiation of an UV laser is employed. In this experiment, it is used the same type of mask throughout the whole trial. It contains devices based on MMI architectures meant to perform the behaviors of the Magic-T and the HWT. It also has some splitters to help characterize the circuits.

Basically, the mask is a glass coverslip with a chromium layer that comprises the devices' designs and which stops UV radiation from transmitting. An amplitude mask is appropriated since this type can write its design directly into the films (samples) with the same dimensions. A phase mask is usually employed for Bragg's networks, and they focus on light diffraction. The thin films are placed over a Si/SiO_2 substrate, and they are constituted of di-ureasil, an organic-inorganic hybrid, doped with zirconium propoxide (ZPO) and methacrylic acid ($McOH$) [4][5][6].

An UV pulsed laser ($\lambda = 248nm$, $PulseDuration = 15ns$), Coherent BraggStar Industrial - High Power Excimer Laser [14], is utilized, so the above described elements highly absorb the radiation at $248nm$ and they compress in the exposed zone. Consequently, this zone will have a higher zirconium's concentration which elevates the refractive index, transforming that zone in waveguides [15]. Hence, controlling the material's exposure to the laser, it is also possible to control the refractive index's variation that it is being generated in the di-ureasil [5].

4.2 Laser Setup

A well-adjusted system of lenses, mirrors, and slits helps the laser navigate through space, and most importantly, it perpendicularly projects the laser into the mask, so the circuits are homogeneously printed instead of being asymmetrical due to the angle of incidence (Figure 4.1).

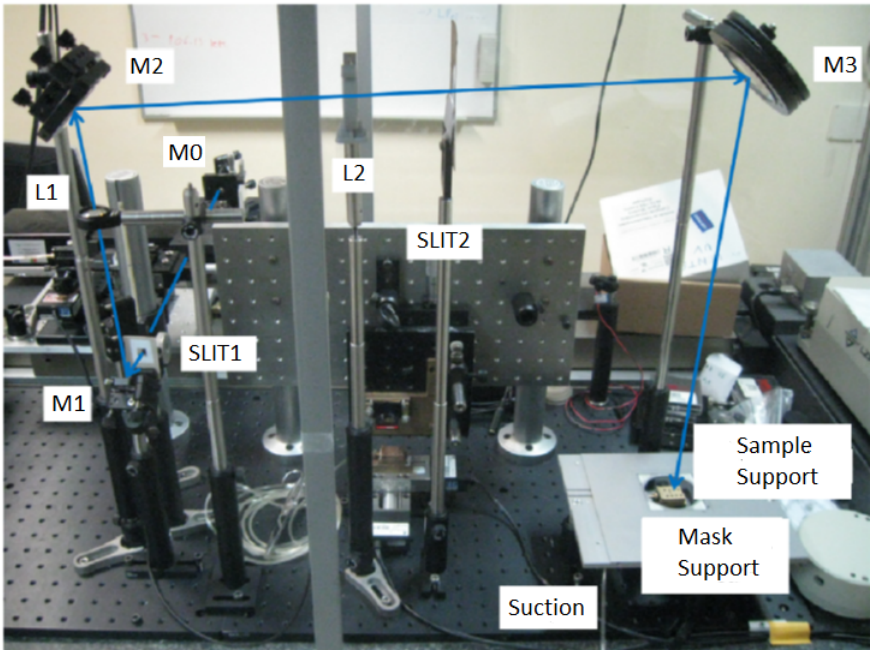

Figure 4.1: Experimental Setup

A simple scheme to help understand the above setup is presented next (Figure 4.2), where Mx are mirrors, Lx are lenses and SLITx are the cardboard areas.

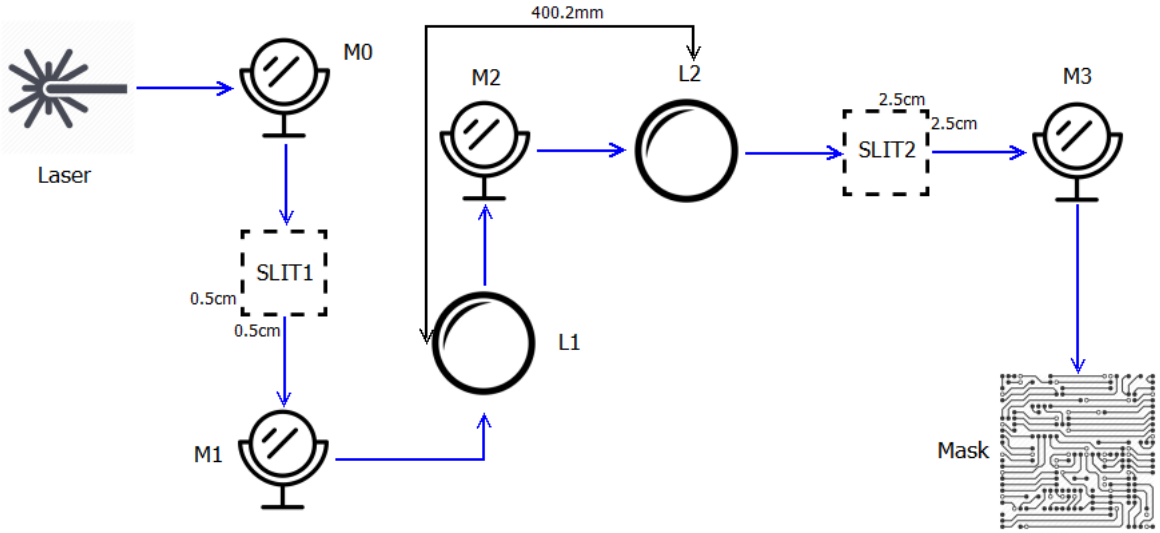

Figure 4.2: Experimental Setup Scheme

The lens L1 is a Newport spr016ar10 ($FocalDistance = 50.2mm$) and the lens L2 is a Newport spr30ar10 ($FocalDistance = 350mm$). The length between these lenses needs to be the sum of their focal distances, $350mm + 50.2mm = 400.2mm$. This distance is hugely significant since it allows the collimation (alignment of the light's rays) of the radiation and the correct amplification of the laser beam. SLIT1 has a dimension of 0.5x0.5 (cm), and its objective is to make the most uniform spot of the laser go through. SLIT2 has a size of 2.5x2.5 (cm), and it is meant to shape the final form that we want the spot to be.

The remaining distances heavily depend on the workspace and how the laser path needs to be set up. A visual inspection of the laser propagation between each component is required during the printing process, to calibrate each one's position.

4.3 Experimental Procedure

For a fixed frequency of $500Hz$ ($RepetitionRate$), different times of exposure with similar energy values are applied to print the designs into the films. The time intervals change, so it is possible to obtain a refractive index contrast to observe which one is closer to the theoretical value, $\eta = 3 * 10^{-3}$.

Before and after each printing process, an energy meter was used to measure the energy located where the mask was supposed to be. When using this device, a frequency of $25Hz$ is established due to security reasons and also because of the device's frequency limitations. However, the energy is identical for both $25Hz$ with the energy meter and $500Hz$ with

the laser radiation, being the latter used for the photolithography process since it is more efficient.

Table 4.1 shows the several trials and their respective values. The arrows mean: Initial Energy/Power → Ending Energy/Power and the formulas used for the Average Power and the Peak Power are, respectively:

$$P_{avg} = \frac{Energy}{PulseDuration} \tag{4.1}$$

$$P_{peak} = \frac{Energy}{RepetitionRate * PulseDuration} \tag{4.2}$$

No. of Tries	**Energy** (μJ)	**Time** (min)	**Average Power** (W)	**Peak Power** (W)
1	363 → 174	12	24k2 → 11k6	48.4 → 23.2
2	174 → 80	10	11k6 → 5k3	23.2 → 10.7
3	327 → 170	8	21k8 → 11k3	43.6 → 22.7
4	350 → 150	14	23k3 → 10k	46.7 → 20.0

Table 4.1: Photolithography Samples Results

After the second trial, it was noticeable that the energy was decreasing during the printing process. For an adequate study of the energy evolution with time, a minute by minute measure of the energy was performed, after the printing process (Table 4.2).

Time (min)	**Energy** (μJ)
0	167
1	169.8
2	170.8
3	172.3
4	173.6
5	174.1

Table 4.2: Energy evolution with Time

It is recognizable that the energy decreases during the printing process. This is due to the temperature's increase inside the laser box and due to the gas pressure as well. Hence, a post-printing stabilization time (around 20-30 minutes) is required so that the energy recovers its losses as the temperature goes back to its ambient value, as it can be observable

in Table 4.2. For the second trial, the stabilization time was not applied, and the film's circuits were not as visible to the naked eye as in the first one. Only using the microscope, it was possible to visualize the lines and numbers that compose the films (Figure 4.3).

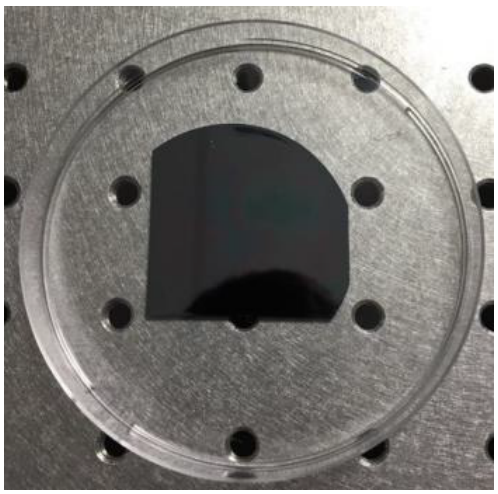

Figure 4.3: One of the resulting samples

Following this experiment, a visual inspection of the samples was performed. Using a Leica DM750M microscope, each circuit was scanned for dust, holes or other impairments that can occur during the exposure to the UV laser (Figure 4.4). Tests of signal coupling on the best circuits will be performed, so the printing process can be validated if the devices' behavior shows to be near what is expected.

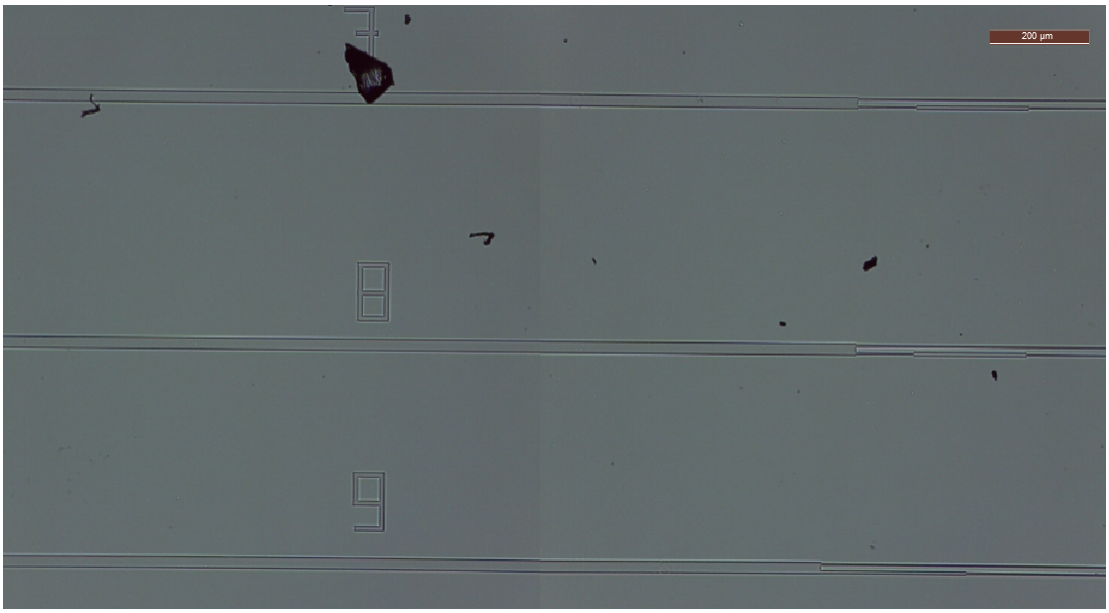

Figure 4.4: Microscopic look at a portion of circuits from sample 4

Later, the sample that achieved the best performance under its respective conditions (time of exposure, energy) would have its printing process repeated with those same conditions, and the refractive index value would be measured through ellipsometry [16].

Chapter 5

Circuits Characterization

In this chapter, the characterization process is explained, and the results of the two-input circuits are discussed. The testing setup is demonstrated as well as the handmade fiber array with which the circuits were tested.

5.1 One-Input Circuits Testing Process

Every required equipment to test one-input circuits is also used to test the multiple-input ones plus some additional components. The description of each equipment is based on [14]. The experimental setup can be seen in Figures 5.1 and 5.2.

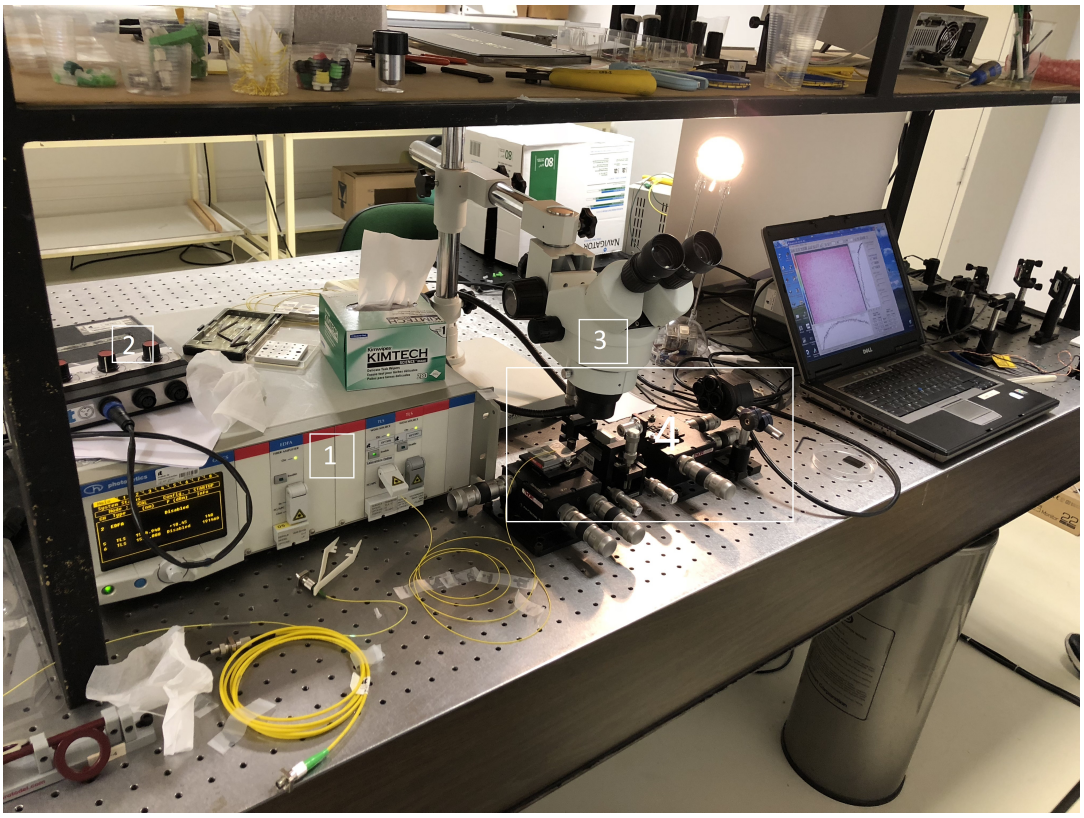

Figure 5.1: Experimental Setup for One-Input Circuits Testing

List of equipment in Figure 5.1:

1. Photonetics OSICS Lasers Module. It can host up to eight pluggable modules, including Tunable Laser Source (TLS). Maximum output power of +13 dBm;

2. Current source of a red laser;

3. Optika SZM-3 Microscope, with external light source needed;

4. Area zoomed in Figure 5.2.

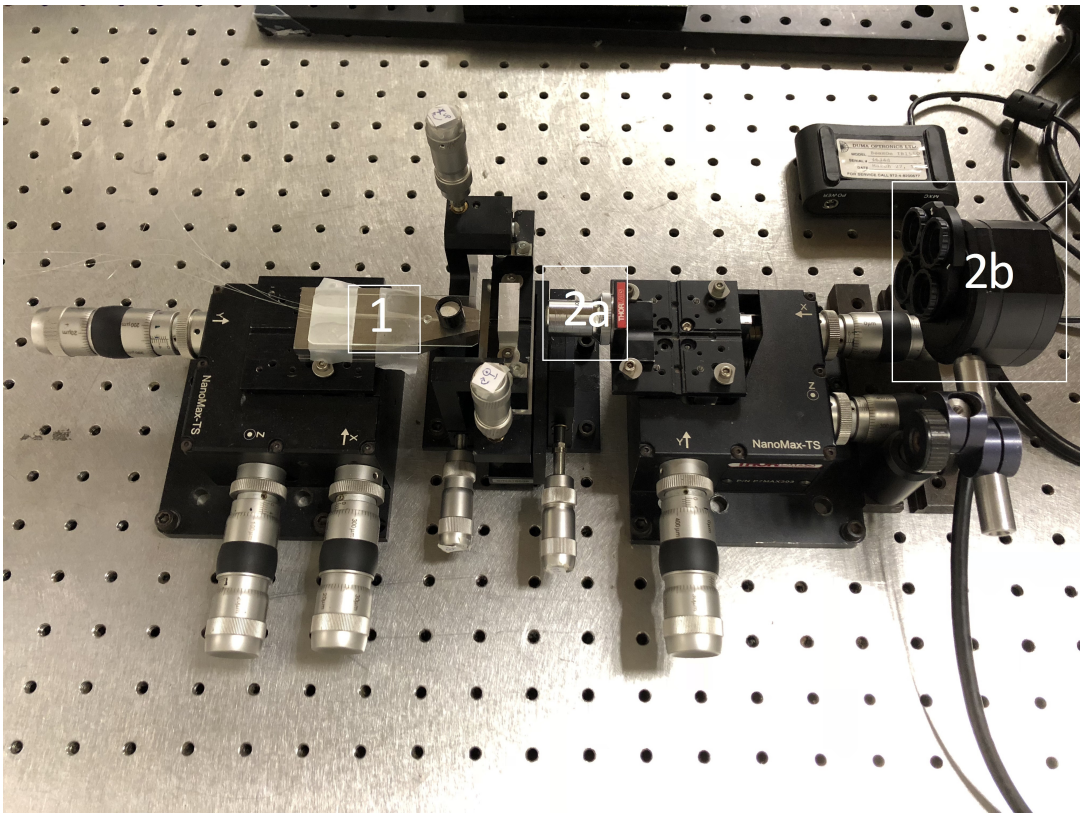

Figure 5.2: Zoomed Testing Area

List of equipment in Figure 5.2:

1. Handmade fiber array (to use only for multiple-input circuits testing);

2. Duma Optronics' Laser Beam Profiler - BeamOn IR1550. This system measures real-time continuous or pulsed laser beams parameters, such as: intensity profiles, beam width, shape, position and power. It uses a Charged-Coupled Detector (CCD) camera head (2a), a built-in filter wheel (2b) and a software which allows the user to analyze the results.

Before the actual testing process starts, some components need to be well prepared. The OSICS module should be turned on early so that it can warm up and deliver the desired output power. The fiber needs to be cleaved, cleaned and taped to the corresponding surface, as seen in the previous figure.

With these pre-testing elements done, the process begins, and a step-by-step method is described:

1. Using a leveler, verify if the place where the sample goes on is well-balanced. If not, use the marked positioners to change the angles until the leveler proves that it is, in fact, balanced;

2. Carefully, clean the sample to use with compressed air. Place it in the rectangular metal spot that is positioned between the fiber and the camera head;

3. Using the microscope, align the fiber with the desired circuit to be tested by rotating the X and Y-axis positioners. The Y-position should be as close as possible to the input so that the light dispersion losses are minimized;

4. Lights off for the remaining of the process. Connect the red laser to the fiber and place a piece of paper in front of the filter wheel. The use of this laser is due to the fact that it is visible to the human eye. This way, it is easier to observe if it is well-aligned with the circuit since by moving the fiber's Z-axis, the red shape in the paper changes. If a uniform circular spot shows up, it means that the laser is above the circuit. By moving it down, the circular form starts to change into stripes (right above the sample), and when a single line is observed, it means it is finally aligned.

5. Using the positioners on the other side of the setup, change the camera's Y and Z-axis positions, so the laser is centered with one of the wheels and rotate the X-axis positioner closer to the sample until the single stripe becomes thinner.

6. Switch the laser source from the red laser to the TLS module of the OSICS mainframe. Set the power around +10 dBm and the wavelength as close as possible to $1550nm$. Enable it, and the software should show the circuit's outputs.

7. In the software, change the shutter speed and gain parameters if necessary to better notice the outputs. Beware of the white spots in each output since that means that the software is overflowed and the values will not be valid. The X-axis of the CCD camera should also be adjusted to obtain more round outputs.

5.1.1 Gaussian Approximation

The best way to analyze the results is to get the values from the software and use MATLAB to process them through a Gaussian approximation, giving us important parameters,

such as: *Full Width at Half Maximum (FWHM)* (μm); *Peak Position* (μm); *Height* (au - normalized values); *Area* (au - normalized values).

There is a way of calculating the area under a Gaussian peak by easy measurements [17]. As it is known, the Gaussian distribution is given by

$$f(x) = \frac{1}{\sigma\sqrt{2\pi}} e^{-\frac{(x-\mu)^2}{2\sigma^2}} \tag{5.1}$$

and the function for a peak is

$$f(x) = \frac{A}{\sigma\sqrt{2\pi}} e^{-\frac{(x-\mu)^2}{2\sigma^2}} \tag{5.2}$$

where A is the area under the curve. The maximum peak height can be found at $x = \mu$, which means that

$$H = f(\mu) = \frac{A}{\sigma\sqrt{2\pi}} e^{-\frac{(\mu-\mu)^2}{2\sigma^2}} = \frac{A}{\sigma\sqrt{2\pi}} \tag{5.3}$$

Hence, the area is proportional to the maximum peak height and the FWHM can be given by

$$FWHM = 2\sigma\sqrt{2ln(2)} \tag{5.4}$$

Therefore, mixing equations 5.3 and 5.4, the area is calculated by

$$Area = \frac{Height * FWHM}{(2\sqrt{2ln(2)}) * (1/\sqrt{2\pi})} \tag{5.5}$$

In the following section, the relative power loss between the beams is also analyzed and it is calculated by

$$RelativePowerLoss(\%) = (1 - \frac{area2}{area1}) * 100 \tag{5.6}$$

where $area2 < area1$. If the relative power loss is between a beam and the total distribution, the fraction's numerator equals the sum of the areas.

5.2 Two-Input Circuits Testing Process

To efficiently test the two-input circuits, some additions to the previous setup must be made. Evidently, a 1x2 power splitter is required to equally divide the power through the two fibers with no external impairments, and the power of the OSICS module is set at +12 dBm.

The other modification is the number of fibers in use since it is going to increase to four (remember that the initial goal of this thesis was also to test four-input circuits). Two problems emerge: how can four fibers be efficiently aligned between each other? And how can it be guaranteed that the phase between them is the same (too much phase difference between fibers can affect the results)? Solutions for both problems are described in the following sub-chapters.

5.2.1 Fiber Array

To make the fiber array, the cladding from four Standard Single-Mode Fibers (SSMFs) is removed. Then, these are very carefully pushed against a clean glass coverslip, and when it looks like they are approximately aligned, they are taped together with two tiny tape stripes, one near their ends and the other a bit back. The length of fibers between the stripes is going to be glued together using a specific glue that sets with an UV-laser pistol. Finally, that length is cleaved right after the spot of glue since there the fibers are as close to each other as possible.

Using the previously mentioned Leica microscope, it is verified that the fibers seem to be glued together (Figure 5.4), even though their ends might be $1\mu m$ or $2\mu m$ in front or before one another. Each fiber has $125\mu m$ of core width which means that the array has a full width of $500\mu m$.

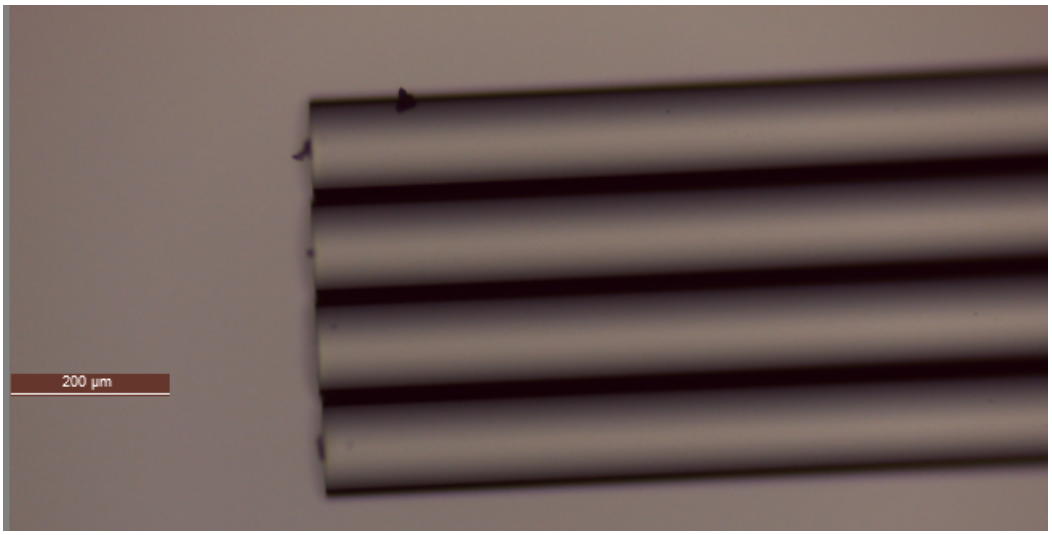

Figure 5.3: Microscope Look at the Fiber Array

Using a Fujikura FSM-60S Fusion Splicer, each fiber is spliced with a fiber pigtail, and the splice sleeve is then heated. To test the circuits, the fibers are taped in a glass coverslip, and a magnet is used to hold them down (see Figure 5.4).

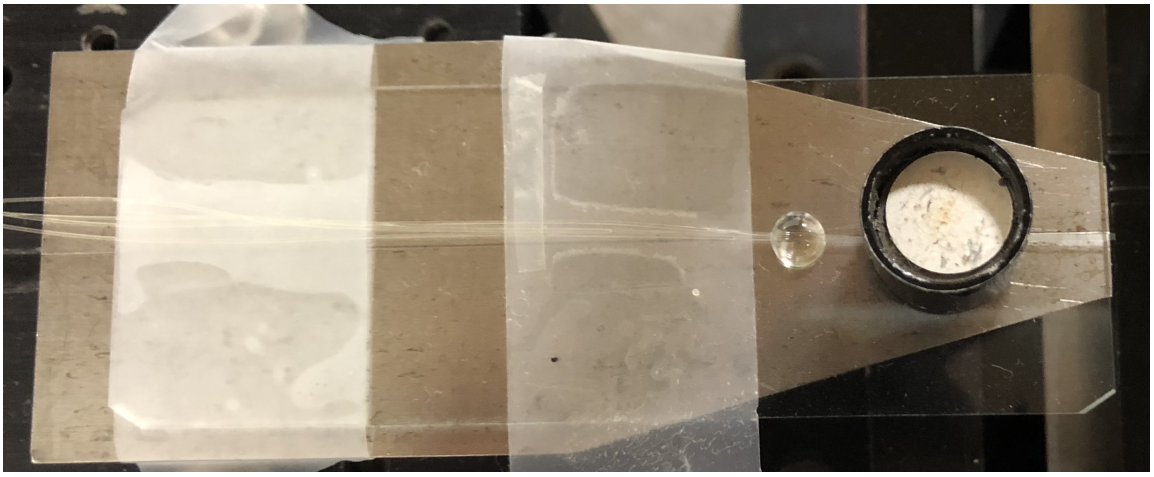

Figure 5.4: Fiber Array in the Setup Area

5.2.2 Phase Variation with Temperature

Even though the fiber array looks good, there is no guarantee that the phase difference (as small as it might be) will not affect the circuits' behavior. Therefore, a study based on Ferreira et al. [18] was performed.

In this article, an integrated photonic-on-a-chip device based on the same hybrid mentioned in this thesis (di-ureasil) was fabricated for temperature sensing. By analyzing this study, an equation that relates temperature to other parameters from the device (wavelength, propagation length, power, ...) was found, and it is given by [18]

$$I = I_0.cos\Big(\frac{2\pi}{\lambda}\frac{dn}{dT}L.\Delta T\Big)^2 \tag{5.7}$$

, where we can define

$$\Delta\phi = \Big(\frac{2\pi}{\lambda}\frac{dn}{dT}L.\Delta T\Big) \tag{5.8}$$

Through this equation and their specifications ($L = 5000\mu m$; $dn/dT = -7 * 10^{-4\circ}C^{-1}$; $\lambda = 1550nm$), the article states that for a change of the cosine argument ($\Delta\phi$) from 0 to $\pi/2$, it is obtained a temperature shift $\Delta T_\pi = 0.055°C$. However, this value is incorrect. By re-doing the math, the correct value is twice the previous one, $\Delta T_\pi = 0.111°C$. For a change from 0 to $\pi/4$, $\Delta T_\pi = 0.055°C$. Using $L = 1mm$, $\Delta T_\pi = 0.277°C$, which means that to change the phase $\pi/4$ in a length of $L = 1mm$, an increase of $0.277°C$ has to be performed on the device.

Even though the type of device is different from the one on this thesis, the temperature change in the same substrate should have similar consequences. Unfortunately, due to the lack of specific material to vary such small values of temperature in even shorter lengths, this approach could not be executed.

Therefore, the test of the following circuits obeys the same procedure as the one-input ones, with the addition of the power splitter and the fiber array as additional setup components. These fibers were re-arrayed with approximate lengths to minimize phase discrimination, but there is no guarantee that inside the power splitter the fibers have the same length. All tests were performed in sample 4 of the previous photolithography process since it was the only one that had all circuits looking intact.

5.2.3 Magic-T using tapers

This circuit employs a simple Magic-T with tapers on both the upper and bottom waveguides (see Figure 5.5). Three variations of the standard test are realized based on which inputs are active: both, upper or bottom.

As stated before, a Gaussian approximation and an analysis of the beams are performed for two different input powers, +7.2 dBm and +11.1 dBm. These are the drawn powers from the OSICS module (which is set at +12 dBm), and the reason behind these two approaches is because the first value had a considerable loss of approximately 5 dBm. The fiber connected to the module could have been damaged in some way, so it was substituted for a new one, and the losses were minimized to less than 1 dBm, hence the repetition of the same tests.

This will affect the circuits' behavior, as it can be verified from the following figures and tables. Have in mind that when the upper or bottom inputs are being separately tested, they are still connected to the power splitter instead of directly connected to the main source.

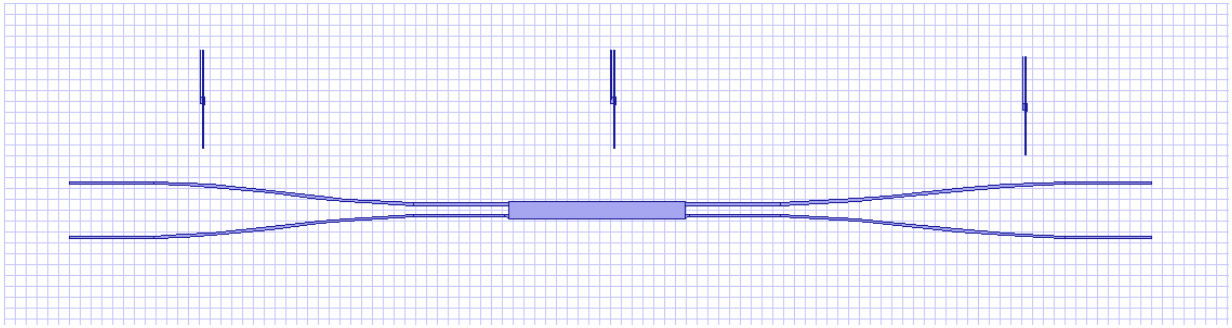

Figure 5.5: Magic-T using tapers

With both inputs drawing the same power (Figures 5.6 to 5.9, Tables 5.1 and 5.2), this circuit should work as most of the ones present in the sample: one output gives the sum of the inputs while the other provides the subtraction (meaning that these last outputs might not even show up sometimes). The upper output should show the subtraction while the bottom output should show the sum. However, if the refractive index of the di-ureasil was correct, these proprieties would be shown in opposite outputs. Note that the left-right scan of the 2D plot graphs corresponds to the bottom-up scan of the heat maps.

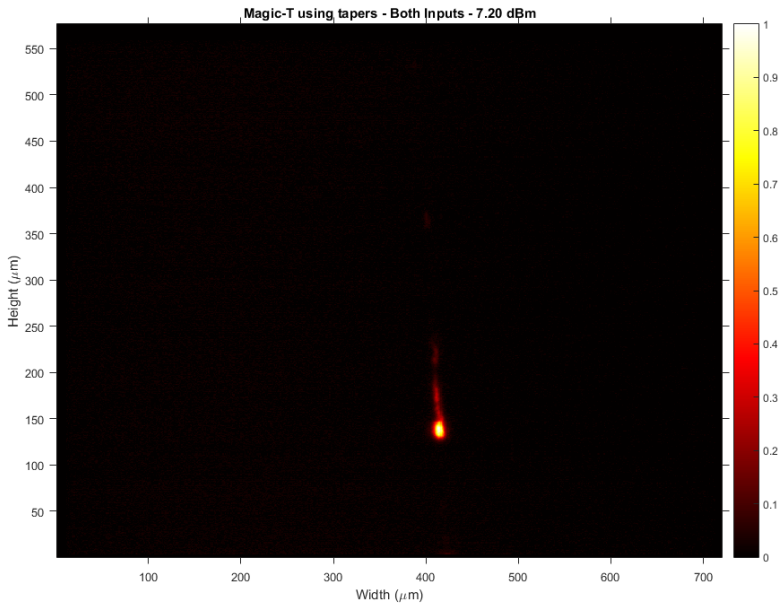

Figure 5.6: Magic-T using tapers - Both Inputs - +7.2 dBm

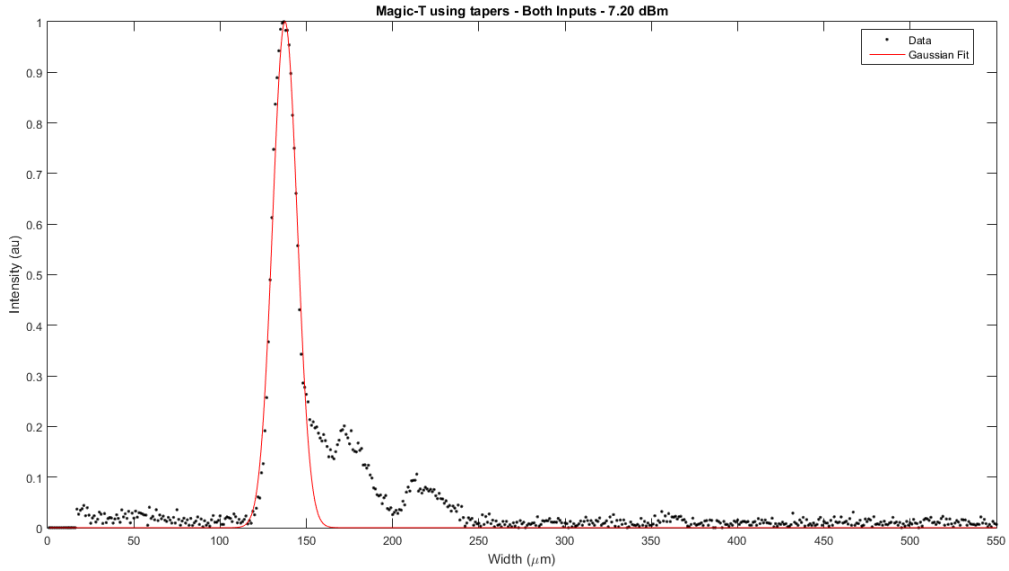

Figure 5.7: Magic-T using tapers - Both Inputs - +7.2 dBm

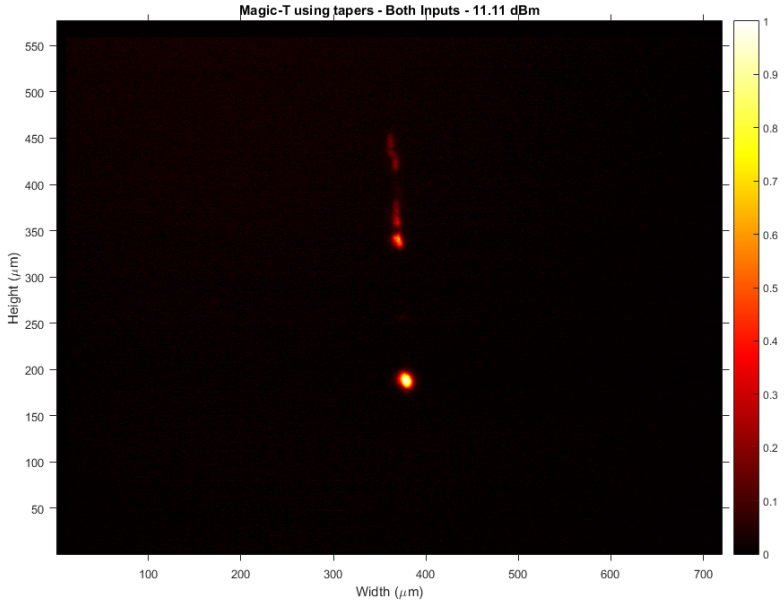

Figure 5.8: Magic-T using tapers - Both Inputs - +11.1 dBm

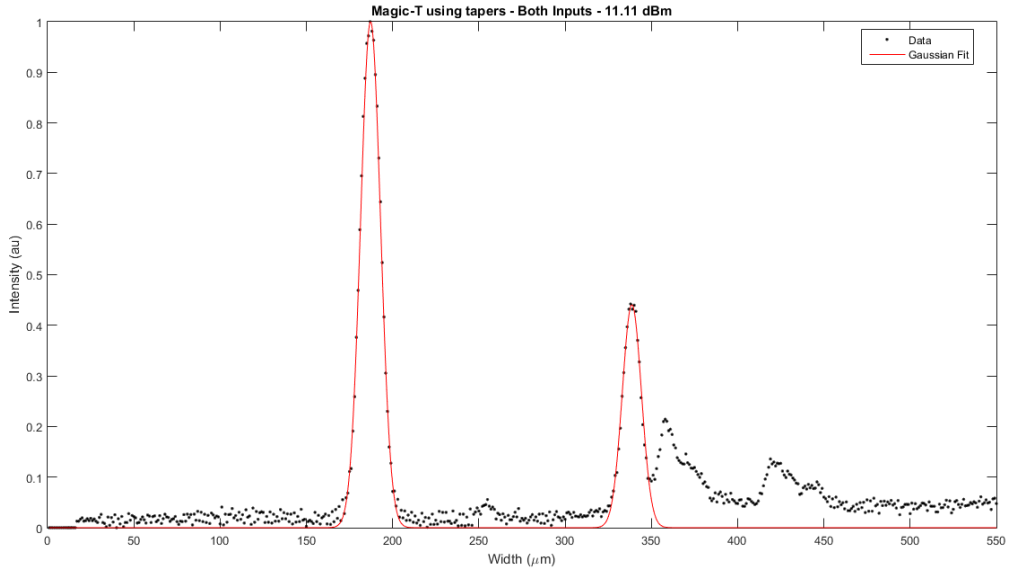

Figure 5.9: Magic-T using tapers - Both Inputs - +11.1 dBm

Beam	FWHM (μm)	Peak Position (μm)	Height (au)	Area (au)
1	16.8535	136.5687	1	17.9400

Table 5.1: Magic-T using tapers - Both Inputs - +7.2 dBm

Beam	FWHM (μm)	Peak Position (μm)	Height (au)	Area (au)
1	13.6364	186.2035	1	14.5155
2	13.2709	337.7086	0.4383	6.1920
	Relative Power Loss			
	Beams	**%**	**dB**	
	1-2	57.3	3.7	
	Total vs 1	29.9	1.54	
	Total vs 2	70.1	5.24	

Table 5.2: Magic-T using tapers - Both Inputs - +11.1 dBm

By observing the figures and tables above, something interesting occurs. When the power drawn from the splitter is +7.2 dBm (+3.6 dBm in the fibers), the upper output (subtraction) does not appear. When the power drawn from the splitter is +11.1 dBm (+5.55 dBm in the fibers), the upper output shows a small amount of power. This proves that with the increase of the input power, the subtraction output will start to have little bits of power that remain from the non-100% efficient subtraction.

In both cases, the expected is proven right. The bottom output shows the sum of the signals and the upper output shows its subtraction. In the first test, only one beam was able to be analyzed, but in the second one, two beams show up, and a relative power loss calculus is possible between them (Table 5.2).

The **Total vs 2** percentage shows how much power beyond the second beam (upper output) the circuit has, in the same way that the **Total vs 1** does for the first beam. The **1-2** percentage shows how much power the first beam has in relation to the second one. Note that the sum of the **Total vs 1** and **Total vs 2** percentages equal 100% and it is also noticeable that the subtraction of the dB values of **Total vs 2** by **Total vs 1** gives the dB value of **1-2**.

When only the upper input is drawing power, the circuit should become a simple splitter. See Figures 5.10 to 5.13 and Tables 5.3 and 5.4.

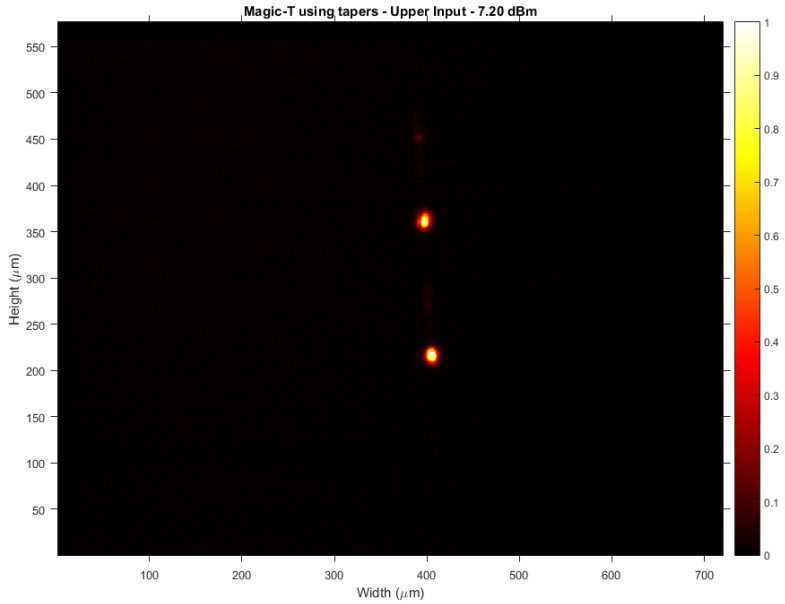

Figure 5.10: Magic-T using tapers - Upper Input - +7.2 dBm

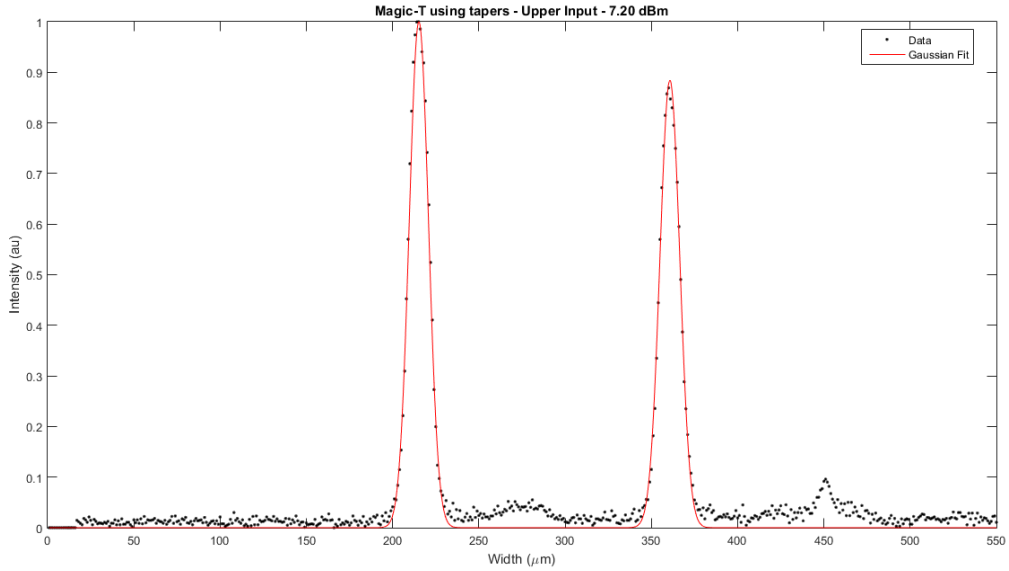

Figure 5.11: Magic-T using tapers - Upper Input - +7.2 dBm

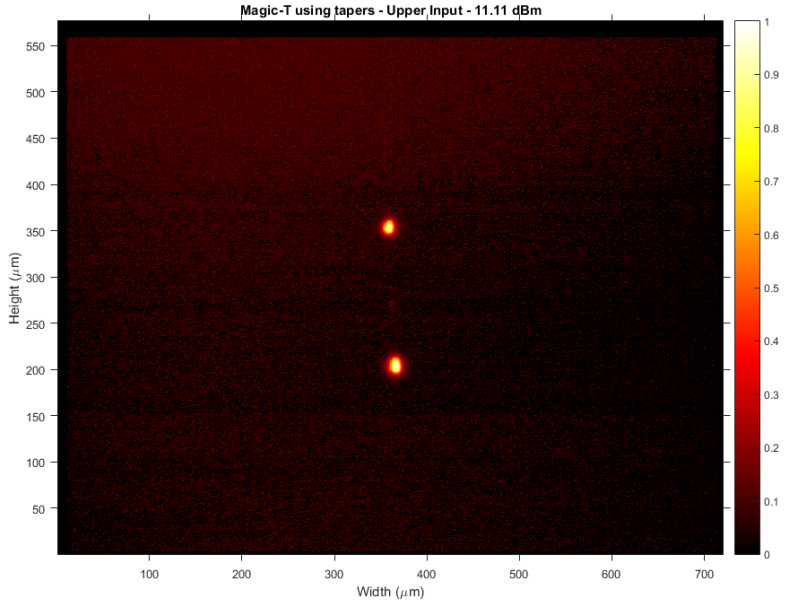

Figure 5.12: Magic-T using tapers - Upper Input - +11.1 dBm

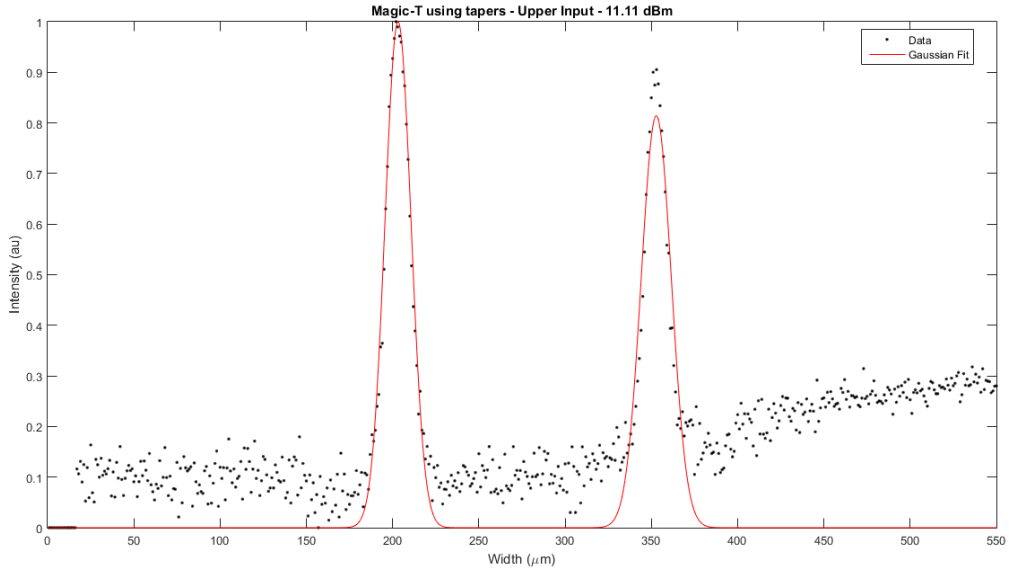

Figure 5.13: Magic-T using tapers - Upper Input - +11.1 dBm

Beam	FWHM (μm)	Peak Position (μm)	Height (au)	Area (au)
1	13.1239	214.2104	1	13.9699
2	13.4925	359.7057	0.8844	12.7022
	Relative Power Loss			
	Beams	**%**	**dB**	
	1-2	9.1	0.41	
	Total vs 1	47.6	2.81	
	Total vs 2	52.4	3.22	

Table 5.3: Magic-T using tapers - Upper Input - +7.2 dBm

Beam	FWHM (μm)	Peak Position (μm)	Height (au)	Area (au)
1	17.7566	202.1180	1	18.9013
2	20.5328	351.8243	0.8142	17.7954
	Relative Power Loss			
	Beams	**%**	**dB**	
	1-2	5.9	0.26	
	Total vs 1	48.5	2.88	
	Total vs 2	51.5	3.14	

Table 5.4: Magic-T using tapers - Upper Input - +11.1 dBm

By observing the tables above, it is verifiable the correct behavior from the circuit. The relative power loss percentages between the beams are very small and the remaining ones are very close to 50%, proving the almost equal division of power.

When only the bottom input is drawing power, it should invert the usual behavior of the circuit i.e. the sum output becomes the subtraction output and vice-versa. See Figures 5.14 to 5.17 and Tables 5.5 and 5.6.

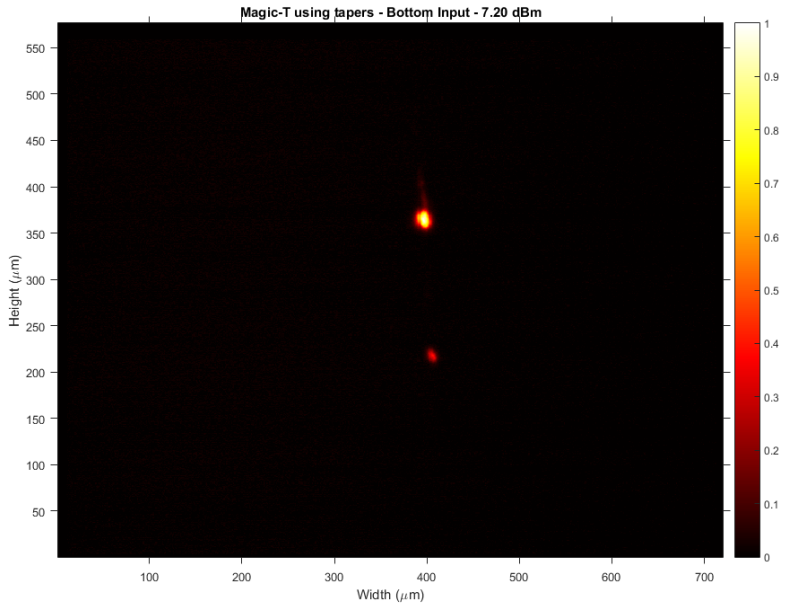

Figure 5.14: Magic-T using tapers - Bottom Input - +7.2 dBm

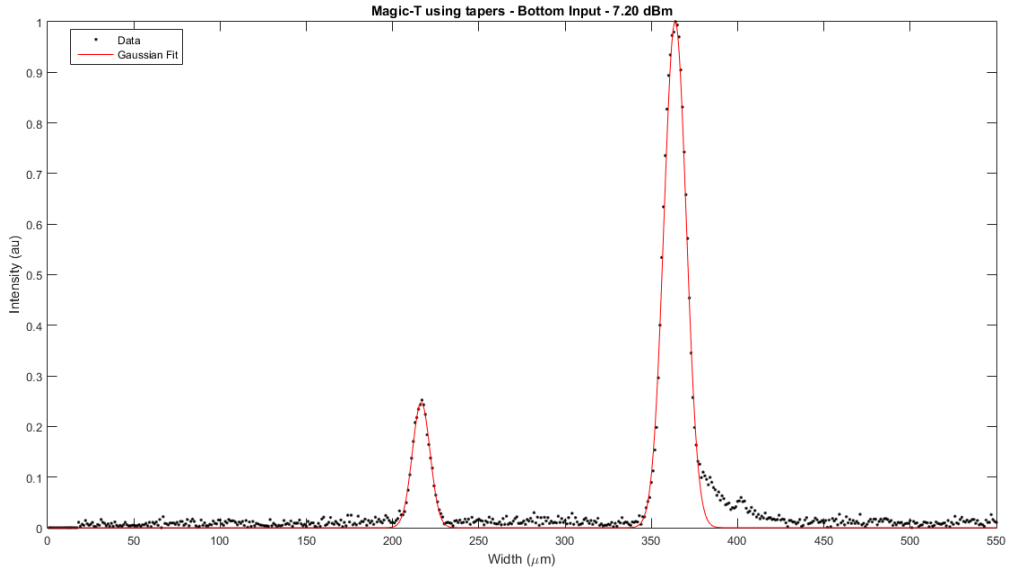

Figure 5.15: Magic-T using tapers - Bottom Input - +7.2 dBm

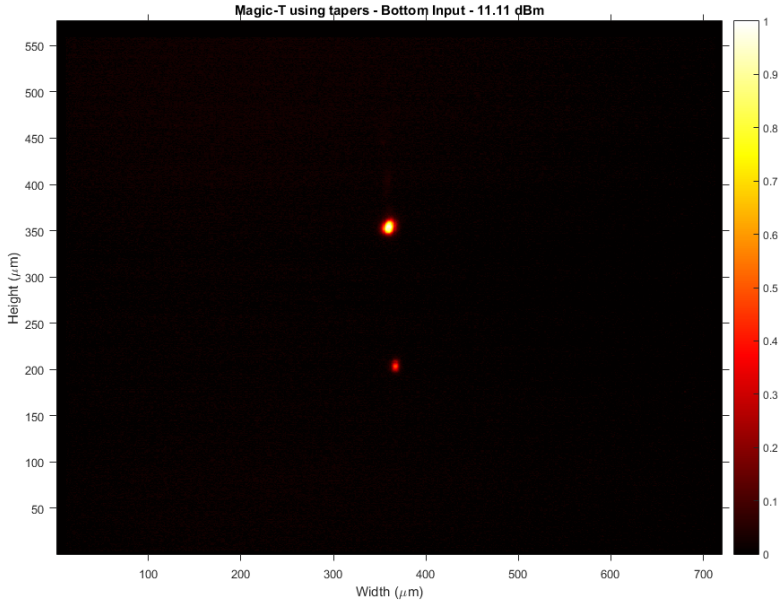

Figure 5.16: Magic-T using tapers - Bottom Input - +11.1 dBm

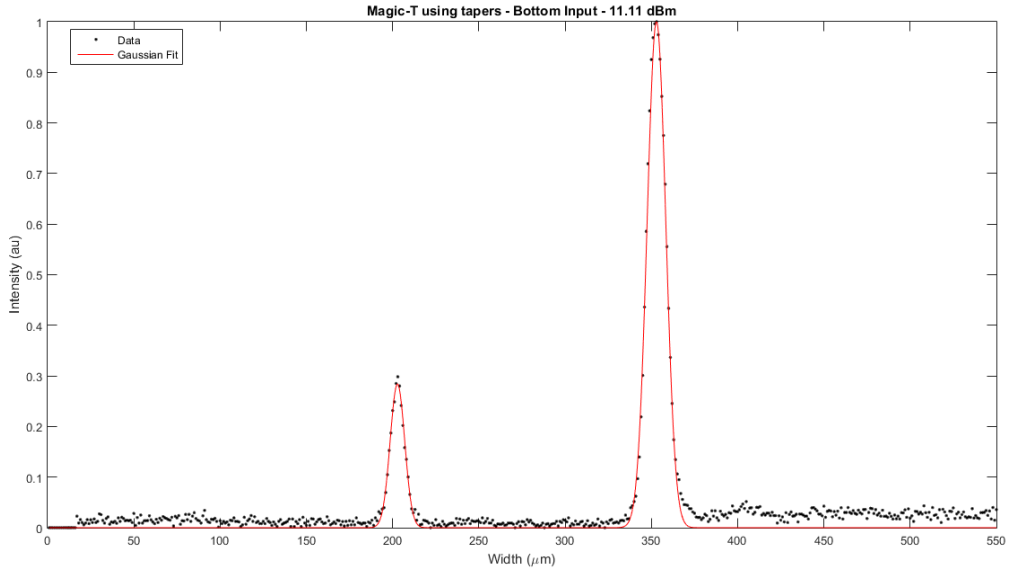

Figure 5.17: Magic-T using tapers - Bottom Input - +11.1 dBm

Beam	FWHM (μm)	Peak Position (μm)	Height (au)	Area (au)
1	12.0747	215.5655	0.2473	3.1789
2	15.2872	362.7546	1	16.2728
	Relative Power Loss			
	Beams	**%**	**dB**	
	1-2	80.5	-7.10	
	Total vs 1	83.7	7.88	
	Total vs 2	16.3	0.77	

Table 5.5: Magic-T using tapers - Bottom Input - +7.2 dBm

Beam	FWHM (μm)	Peak Position (μm)	Height (au)	Area (au)
1	9.9177	201.7840	0.2839	2.9972
2	12.7098	351.9389	1	13.5291
	Relative Power Loss			
	Beams	**%**	**dB**	
	1-2	77.8	-6.54	
	Total vs 1	81.9	7.42	
	Total vs 2	18.1	0.87	

Table 5.6: Magic-T using tapers - Bottom Input - +11.1 dBm

Both tests have similar yet expected results. Since only one input is being used, the difference in input power is not so noticeable (the other input has no power at all). The inverted behavior is accomplished and the circuit goes through all tests as it should.

5.2.4 Magic-T using detached 1x1 MMI device

This circuit uses a 1x1 MMI device detached from the Magic-T (Figure 5.18) and the same testing procedure is followed. This should demonstrate the usual behavior (sum and sub), even when only one of the inputs is on, but with greater efficiency for higher input power values. The 1x1 MMI brings the same delay to the circuit as seen before with the tapers. The difference between a detached and attached MMI component will be demonstrated in the next section.

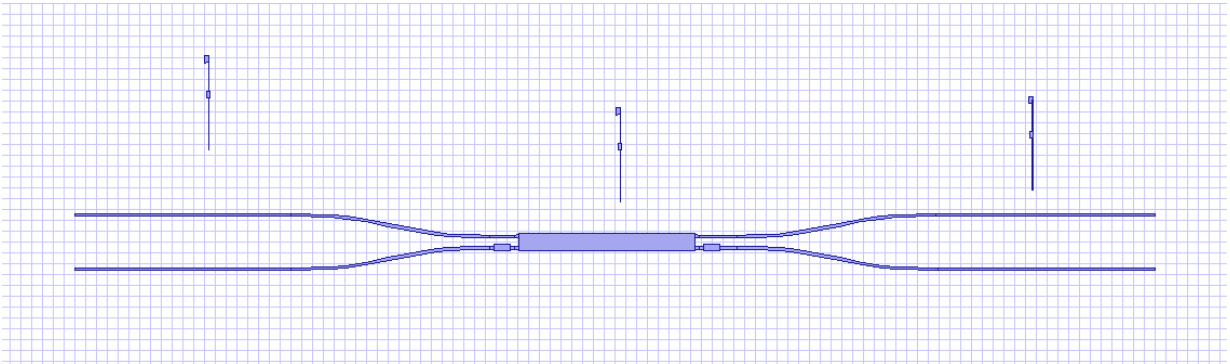

Figure 5.18: Magic-T using detached 1x1 MMI device

With both inputs drawing power, the sum of the input signals should appear in the bottom output while the sub should show up in the upper one. See Figures 5.19 to 5.22 and Tables 5.7 and 5.8.

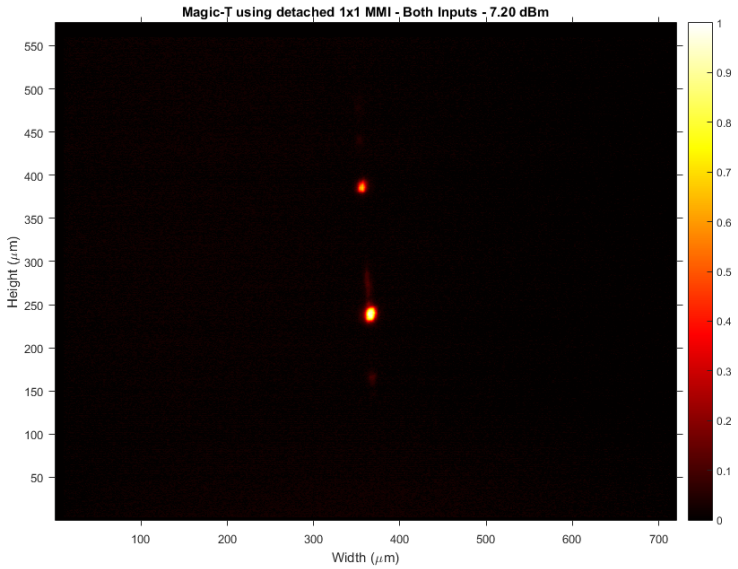

Figure 5.19: Magic-T using detached 1x1 MMI device - Both Inputs - +7.2 dBm

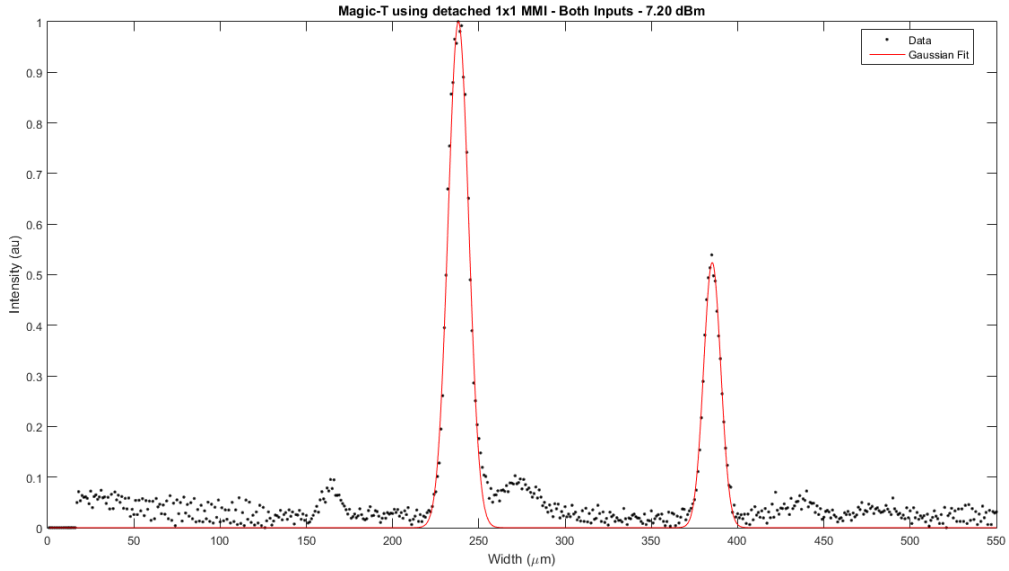

Figure 5.20: Magic-T using detached 1x1 MMI device - Both Inputs - +7.2 dBm

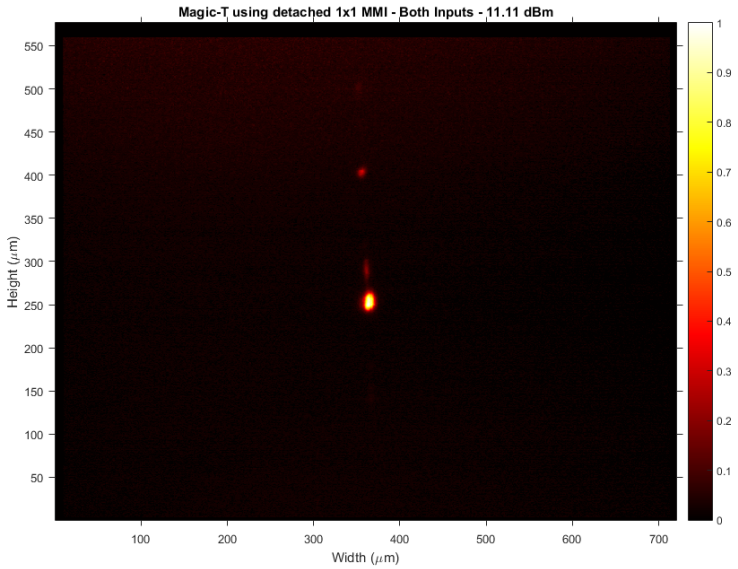

Figure 5.21: Magic-T using detached 1x1 MMI device - Both Inputs - +11.1 dBm

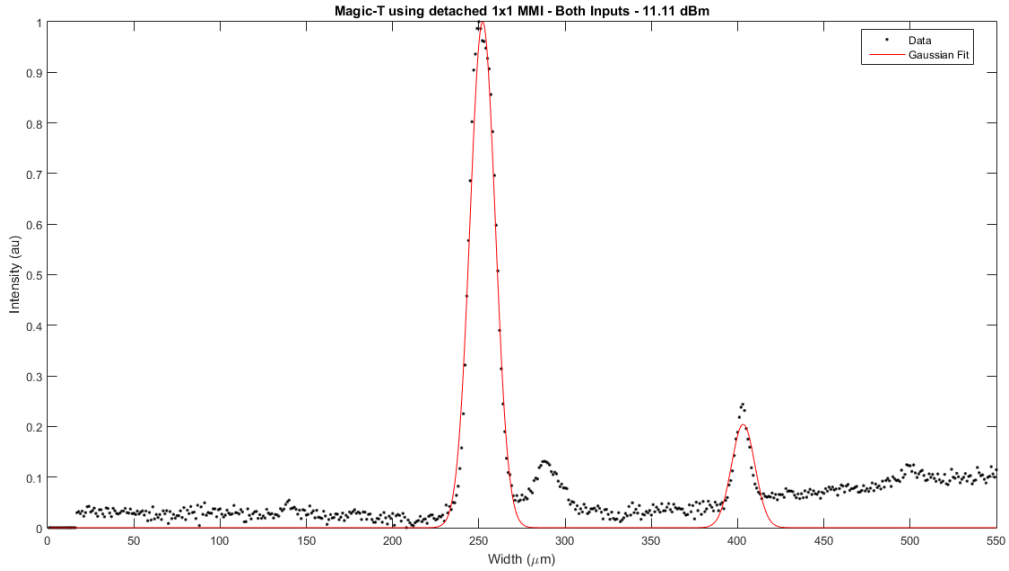

Figure 5.22: Magic-T using detached 1x1 MMI device - Both Inputs - +11.1 dBm

Beam	FWHM (μm)	Peak Position (μm)	Height (au)	Area (au)
1	14.0914	237.1248	1	14.9998
2	11.6753	384.2500	0.5242	6.5143
	Relative Power Loss			
	Beams	**%**	**dB**	
	1-2	56.6	3.63	
	Total vs 1	30.3	1.57	
	Total vs 2	69.7	5.19	

Table 5.7: Magic-T using detached 1x1 MMI device - Both Inputs - +7.2 dBm

Beam	FWHM (μm)	Peak Position (μm)	Height (au)	Area (au)
1	17.5922	250.9684	0.9999	18.7239
2	10.8238	401.6718	0.2394	2.7586
	Relative Power Loss			
	Beams	**%**	**dB**	
	1-2	85.3	8.33	
	Total vs 1	12.8	0.59	
	Total vs 2	87.2	8.93	

Table 5.8: Magic-T using detached 1x1 MMI device - Both Inputs - +11.1 dBm

The results are expected for both cases of input powers. The test with the higher input power was more efficient due to the addition of the MMI device, as it can be seen by the difference in the relative power loss between both cases. With +7.2 dBm, the **Total vs 2** has a 69.7% while for +11.1 dBm, the same parameter has a 87.2%, proving that it was more efficient doing the sum and sub of the input signals.

When the upper input is the only one active, the circuit's behavior should follow the same mechanism as in with both inputs on. However, the difference between the input powers should be almost null since there is no other input to counterbalance the sum and sub. See Figures 5.23 to 5.26 and Tables 5.9 and 5.10.

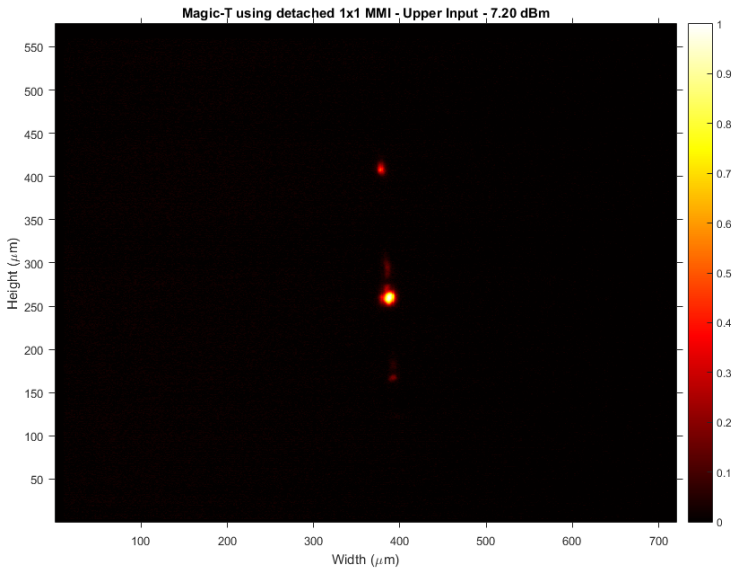

Figure 5.23: Magic-T using detached 1x1 MMI device - Upper Input - +7.2 dBm

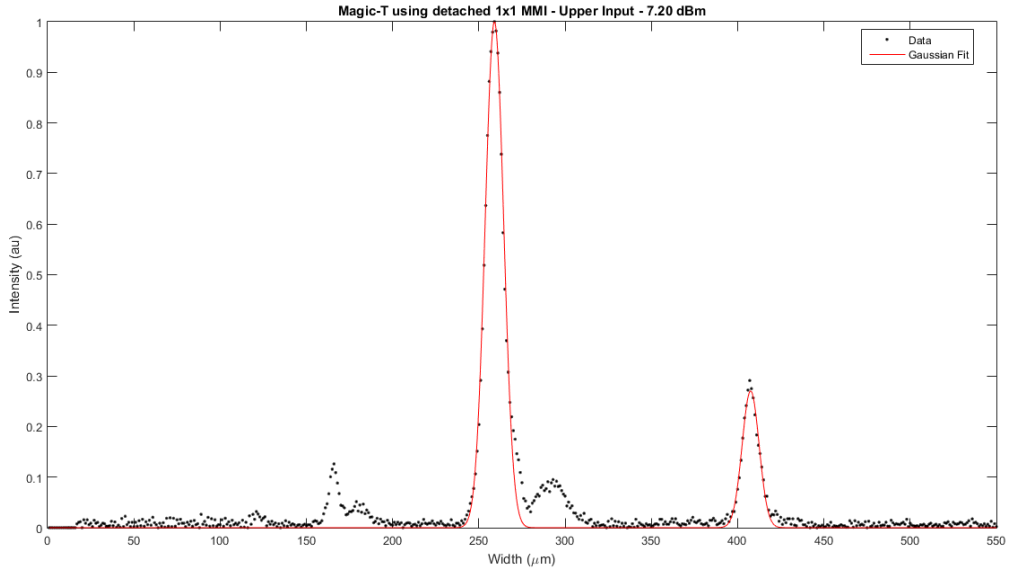

Figure 5.24: Magic-T using detached 1x1 MMI device - Upper Input - +7.2 dBm

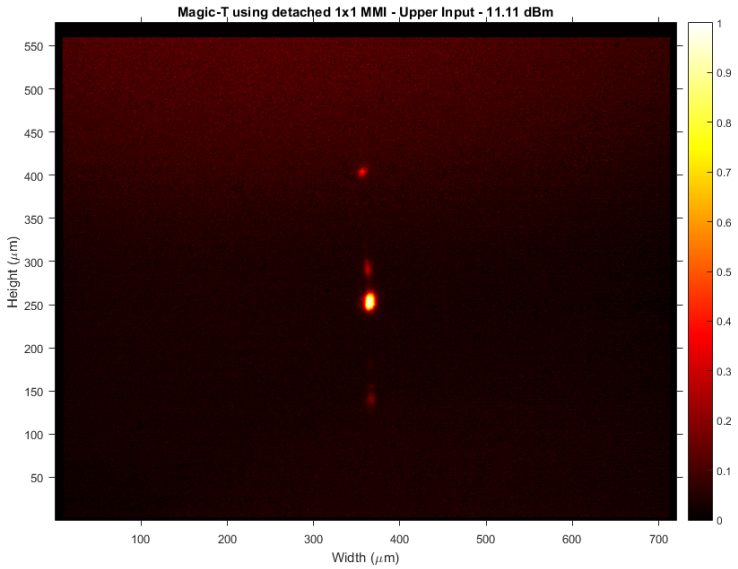

Figure 5.25: Magic-T using detached 1x1 MMI device - Upper Input - +11.1 dBm

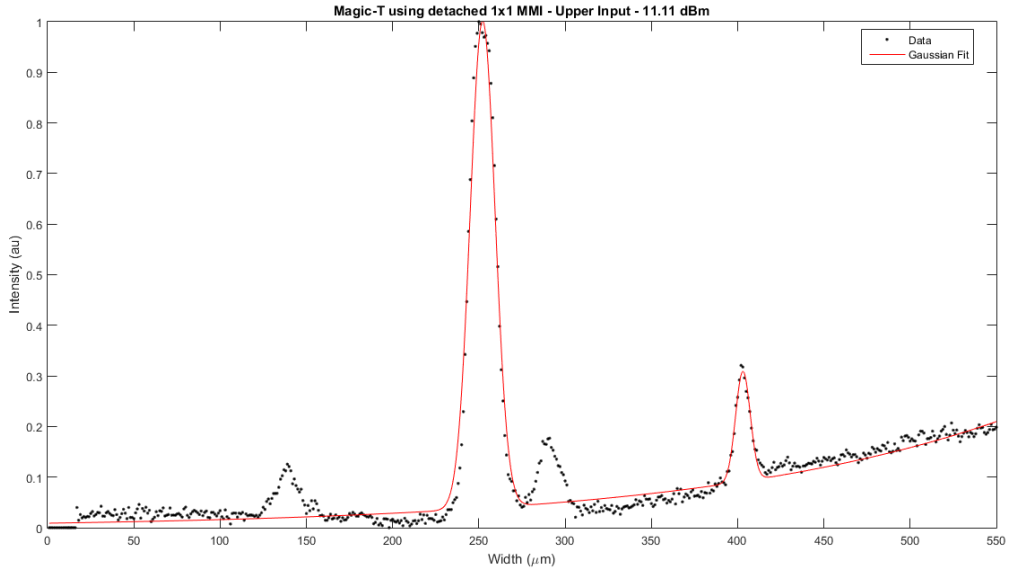

Figure 5.26: Magic-T using detached 1x1 MMI device - Upper Input - +11.1 dBm

Beam	FWHM (μm)	Peak Position (μm)	Height (au)	Area (au)
1	12.6081	258.0088	1	13.4210
2	11.5877	406.5166	0.2703	3.3342
	Relative Power Loss			
	Beams	**%**	**dB**	
	1-2	75.2	6.06	
	Total vs 1	19.9	0.96	
	Total vs 2	80.1	7.01	

Table 5.9: Magic-T using detached 1x1 MMI device - Upper Inputs - +7.2 dBm

Beam	FWHM (μm)	Peak Position (μm)	Height (au)	Area (au)
1	17.5104	251.1724	1	18.6686
2	13.3600	402.0752	0.3089	4.3927
	Relative Power Loss			
	Beams	**%**	**dB**	
	1-2	76.5	6.29	
	Total vs 1	19.0	0.92	
	Total vs 2	81.0	7.21	

Table 5.10: Magic-T using detached 1x1 MMI device - Upper Input - +11.1 dBm

As theoretically predicted, the results show the same behavior with only the upper input and with both inputs on. However, it is noticeable by observing Figure 5.25, that there is a lot more noise coming through the software (red-ish instead of black background). This is due to the higher input power but could also be related with dust, some minor impairments in the waveguides of the circuit or even with the MMI devices.

As seen in the circuit with only the Magic-T plus tapers, when the bottom input is the only input connected to the splitter, the usual behavior of the device inverts. In this case, the upper output becomes the sum port and the bottom output subtracts the input signals. See Figures 5.27 to 5.30 and Tables 5.11 and 5.12.

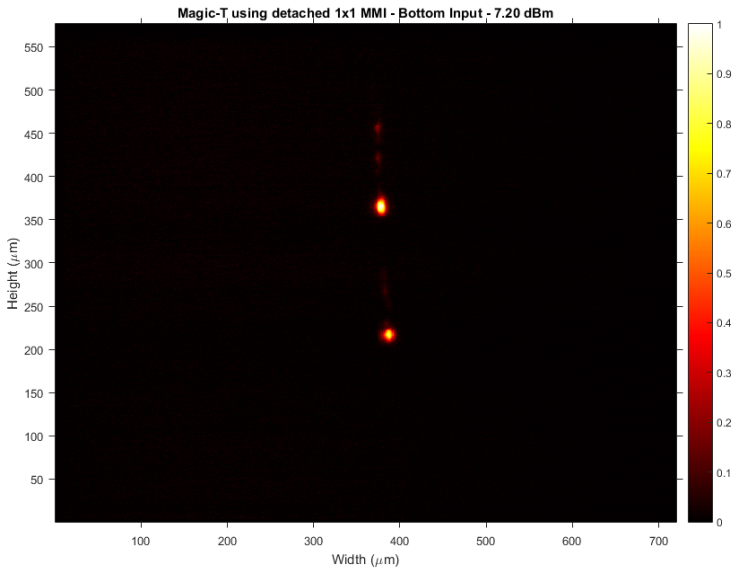

Figure 5.27: Magic-T using detached 1x1 MMI device - Bottom Input - +7.2 dBm

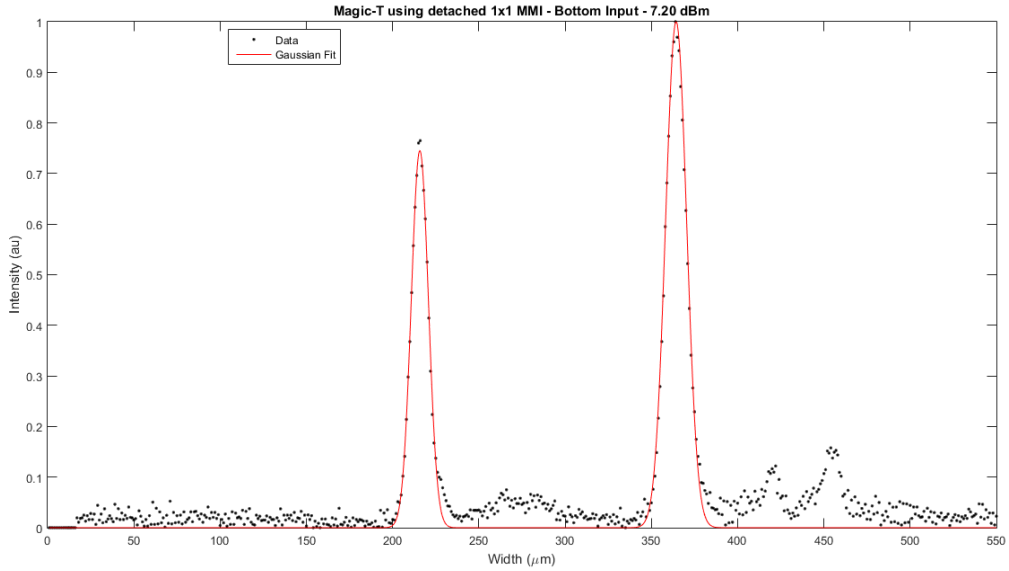

Figure 5.28: Magic-T using detached 1x1 MMI device - Bottom Input - +7.2 dBm

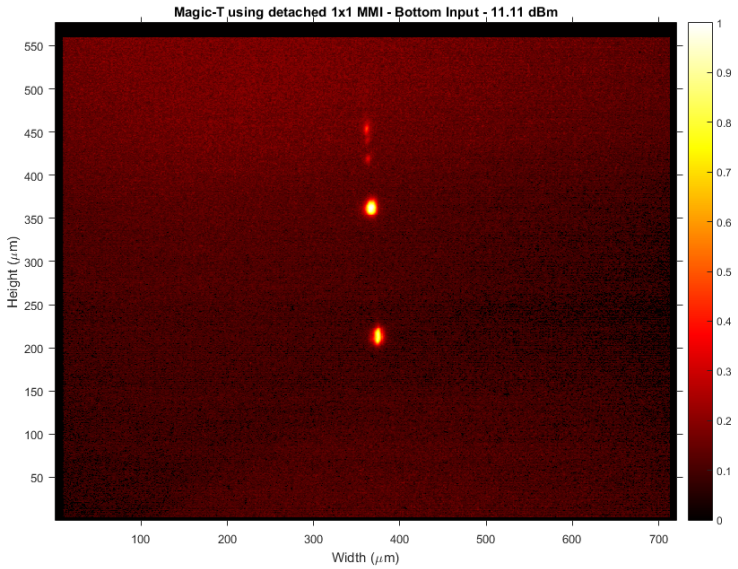

Figure 5.29: Magic-T using detached 1x1 MMI device - Bottom Input - +11.1 dBm

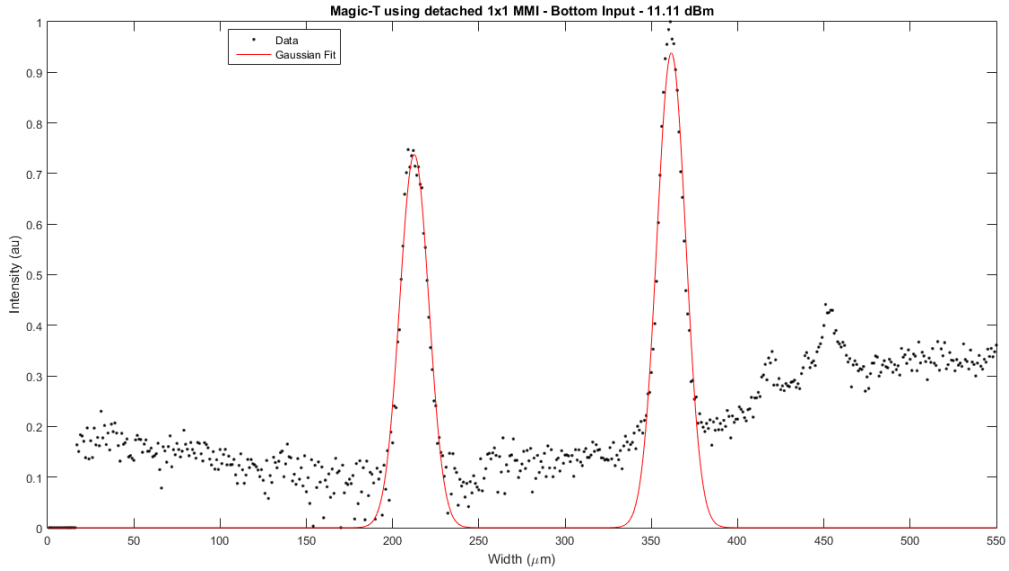

Figure 5.30: Magic-T using detached 1x1 MMI device - Bottom Input - +11.1 dBm

Beam	FWHM (μm)	Peak Position (μm)	Height (au)	Area (au)
1	11.6628	214.7665	0.7455	9.2551
2	14.3599	363.3293	1	15.2856
	Relative Power Loss			
	Beams	**%**	**dB**	
	1-2	39.5	-2.18	
	Total vs 1	62.3	4.24	
	Total vs 2	37.7	2.06	

Table 5.11: Magic-T using detached 1x1 MMI device - Bottom Inputs - +7.2 dBm

Beam	FWHM (μm)	Peak Position (μm)	Height (au)	Area (au)
1	19.8638	211.5308	0.7375	15.5948
2	19.7618	360.5649	0.9383	19.7380
	Relative Power Loss			
	Beams	**%**	**dB**	
	1-2	21.0	-1.02	
	Total vs 1	55.9	3.56	
	Total vs 2	44.1	2.53	

Table 5.12: Magic-T using detached 1x1 MMI device - Bottom Input - +11.1 dBm

The circuit works as expected and inverts the traditional behavior for both cases, but with much less efficiency. The device almost simulates a power splitter, especially with the higher input power, where the relative power loss percentages are near 50%.

In the first test, even though the height of the bottom output (beam 1) is high, its FWHM and area are small, hence the difference in relative power losses percentages between the beams (**Total vs 1** = 62.3%, **Total vs 2** = 37.7%). Nevertheless, in the second test, the high input power causes noise (hence the red background in Figure 5.29) and the values may not be entirely valid.

This circuit can be improved with a simple modification ...

5.2.5 Magic-T using attached 1x1 MMI device

In the previous circuit, the MMI devices were detached from the Magic-T. The test with both inputs turned on, performed as expected, but for higher input power values noise was still an issue. By attaching the MMI to the Magic-T (Figure 5.31), the losses between the components are minimized and the efficiency should maintain its high levels.

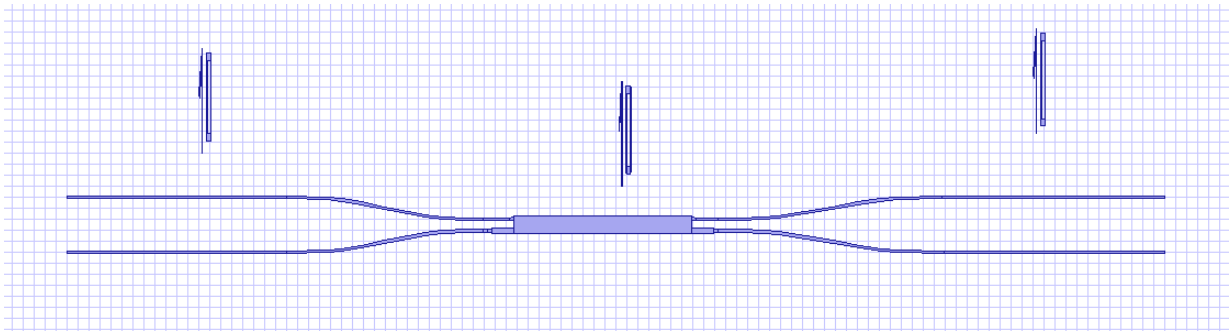

Figure 5.31: Magic-T using attached 1x1 MMI device

Additionally, the main difference is that the usual behavior inverts compared with the circuit with the detached MMI devices. See Figures 5.32 to 5.35 and Tables 5.13 and 5.14.

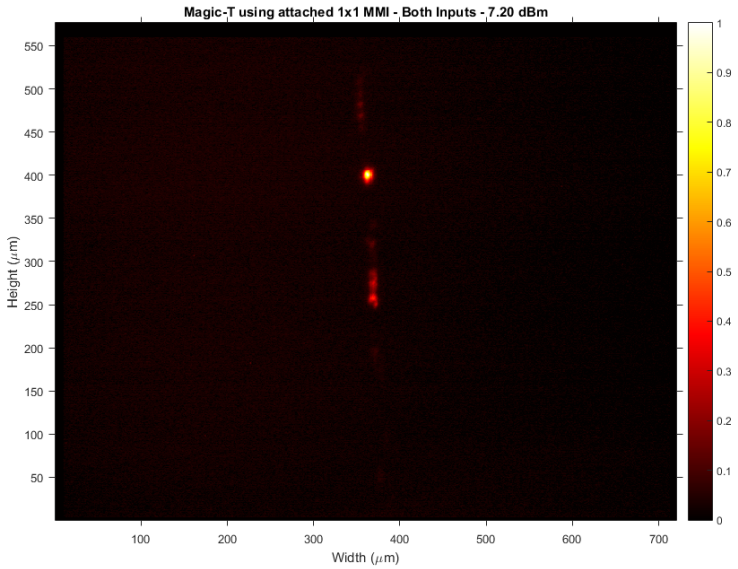

Figure 5.32: Magic-T using attached 1x1 MMI device - Both Inputs - +7.2 dBm

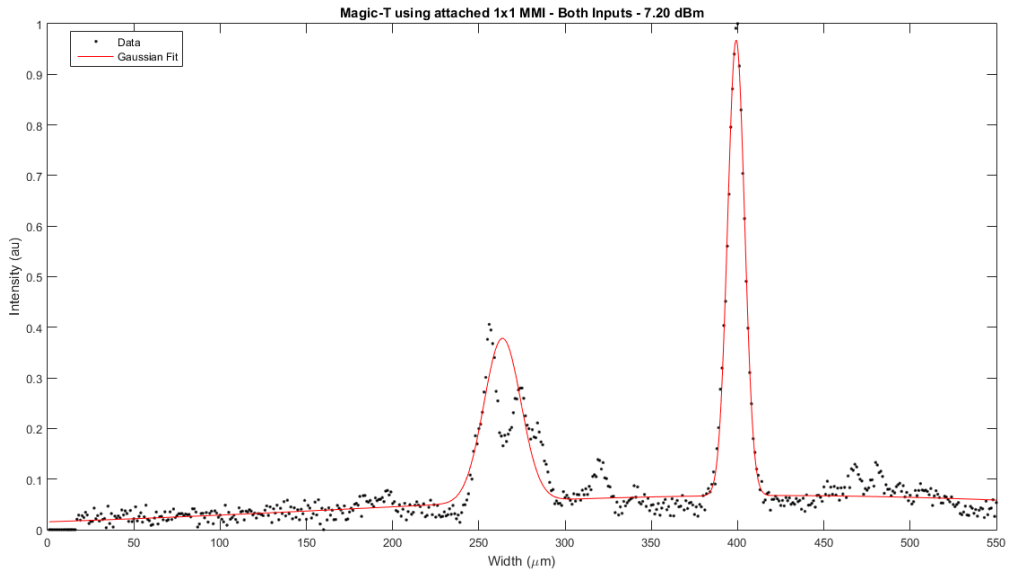

Figure 5.33: Magic-T using attached 1x1 MMI device - Both Inputs - +7.2 dBm

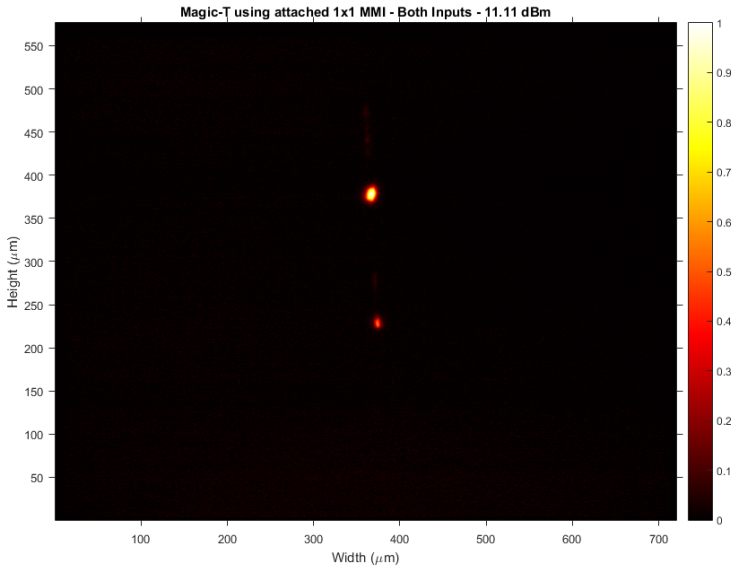

Figure 5.34: Magic-T using attached 1x1 MMI device - Both Inputs - +11.1 dBm

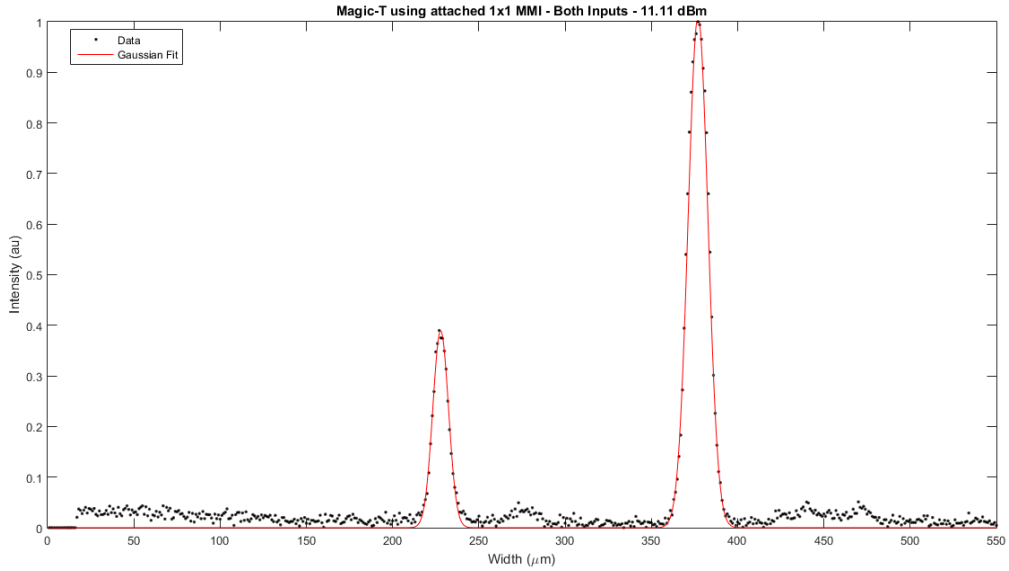

Figure 5.35: Magic-T using attached 1x1 MMI device - Both Inputs - +11.1 dBm

Beam	FWHM (μm)	Peak Position (μm)	Height (au)	Area (au)
1	28.4363	262.7009	0.3782	11.4484
2	12.1962	398.1311	0.9677	12.5637
	Relative Power Loss			
	Beams	**%**	**dB**	
	1-2	8.9	-0.40	
	Total vs 1	52.3	3.21	
	Total vs 2	47.7	2.81	

Table 5.13: Magic-T using attached 1x1 MMI device - Both Inputs - +7.2 dBm

Beam	FWHM (μm)	Peak Position (μm)	Height (au)	Area (au)
1	10.7290	226.8363	0.3893	4.4457
2	13.5489	376.0409	1	14.5574
	Relative Power Loss			
	Beams	**%**	**dB**	
	1-2	69.5	-5.16	
	Total vs 1	76.6	6.31	
	Total vs 2	23.4	1.16	

Table 5.14: Magic-T using attached 1x1 MMI device - Both Inputs - +11.1 dBm

With +7.2 dBm, the circuit is not as efficient. It can be seen in Figure 5.32 that the usual round shapes of the outputs were not possible to obtain due to the low input power, but also due to some dust and impairments near the output waveguides. However, it does demonstrate the expected inverted behavior comparing with the previous circuit.

Nevertheless, in the second test, everything performed as expected. There are two clear sum and sub outputs, plus the inverted behavior is accomplished with no signs of noise and great efficiency.

With the upper input being the only one drawing power, it is going to invert the circuit's behavior when both inputs are on. See Figures 5.36 to 5.39 and Tables 5.15 and 5.16.

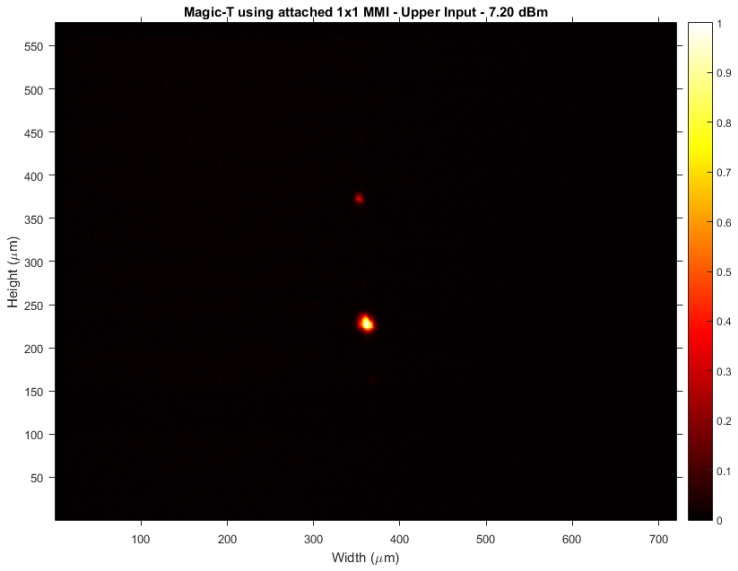

Figure 5.36: Magic-T using attached 1x1 MMI device - Upper Input - +7.2 dBm

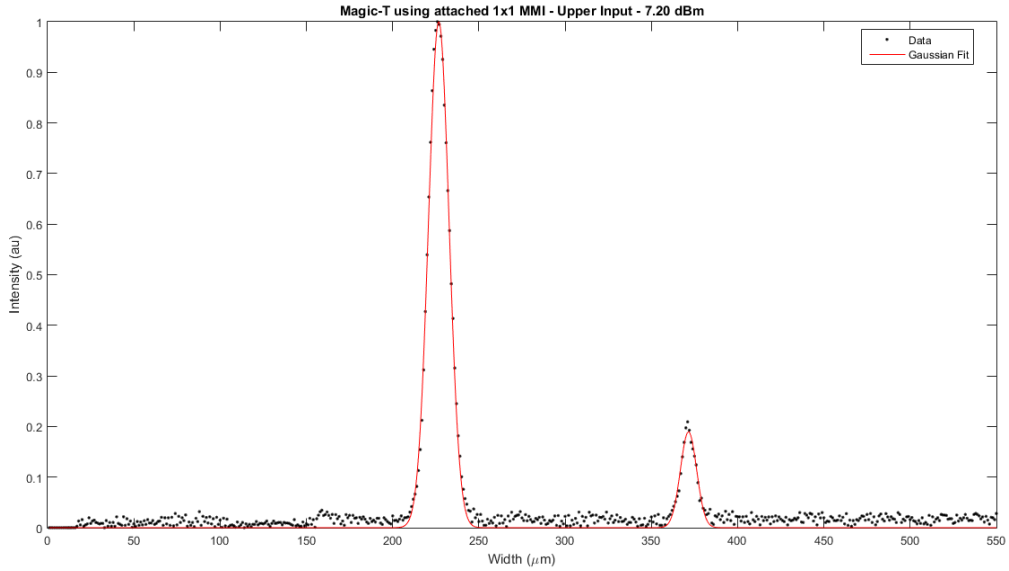

Figure 5.37: Magic-T using attached 1x1 MMI device - Upper Input - +7.2 dBm

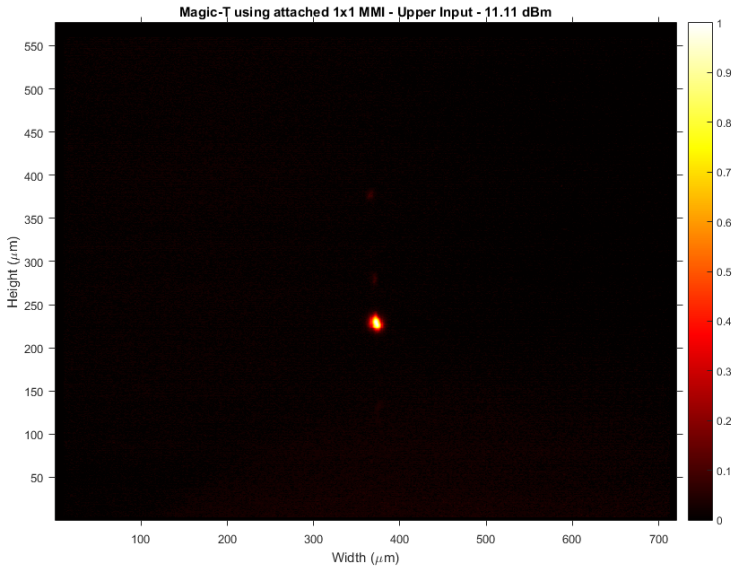

Figure 5.38: Magic-T using attached 1x1 MMI device - Upper Input - +11.1 dBm

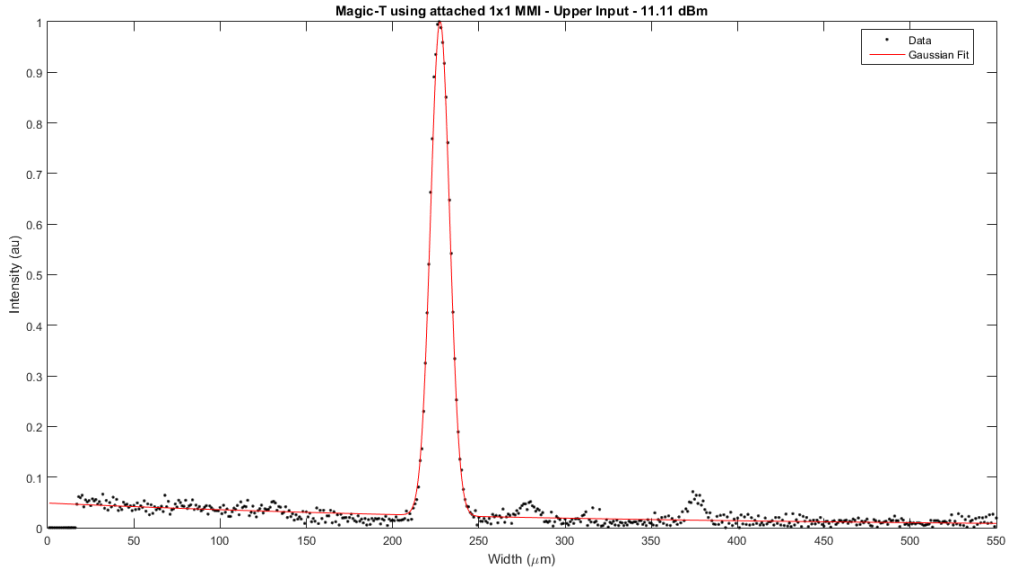

Figure 5.39: Magic-T using attached 1x1 MMI device - Upper Input - +11.1 dBm

Beam	FWHM (μm)	Peak Position (μm)	Height (au)	Area (au)
1	14.0223	225.7460	1	14.9263
2	11.0772	370.5229	0.1894	2.2332
	Relative Power Loss			
	Beams	**%**	**dB**	
	1-2	85.0	8.24	
	Total vs 1	13.0	0.60	
	Total vs 2	87.0	8.86	

Table 5.15: Magic-T using attached 1x1 MMI device - Upper Input - +7.2 dBm

Beam	FWHM (μm)	Peak Position (μm)	Height (au)	Area (au)
1	13.2750	226.4995	1	14.1418

Table 5.16: Magic-T using attached 1x1 MMI device - Upper Input - +11.1 dBm

Both tests accomplish what was predicted. The circuit's behavior is inverted in relation to the one witnessed when both inputs are on.

In the first test, the low input power did not cause any problems, even though the subtraction is not 100% efficient. However, in the second test, the sum and sub mechanism is as efficient as it can be and it only shows the sum port, demonstrating that the whole input signal went through the sum output.

When the bottom input is the only one active, it should have a similar behavior to the first case (both inputs on). In the previous circuit, the results were weakened by some impairments, but those were completely removed partially due to the attachment of the MMI components to the Magic-T. See Figures 5.40 to 5.43 and Tables 5.17 and 5.18.

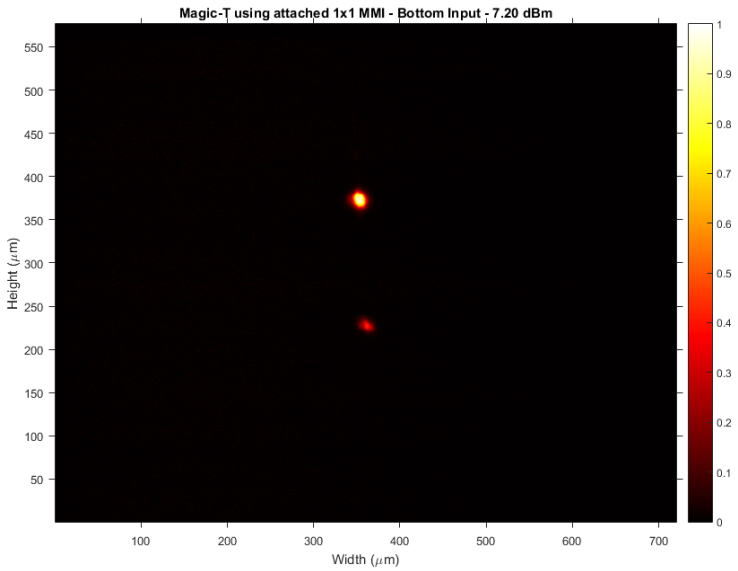

Figure 5.40: Magic-T using attached 1x1 MMI device - Bottom Input - +7.2 dBm

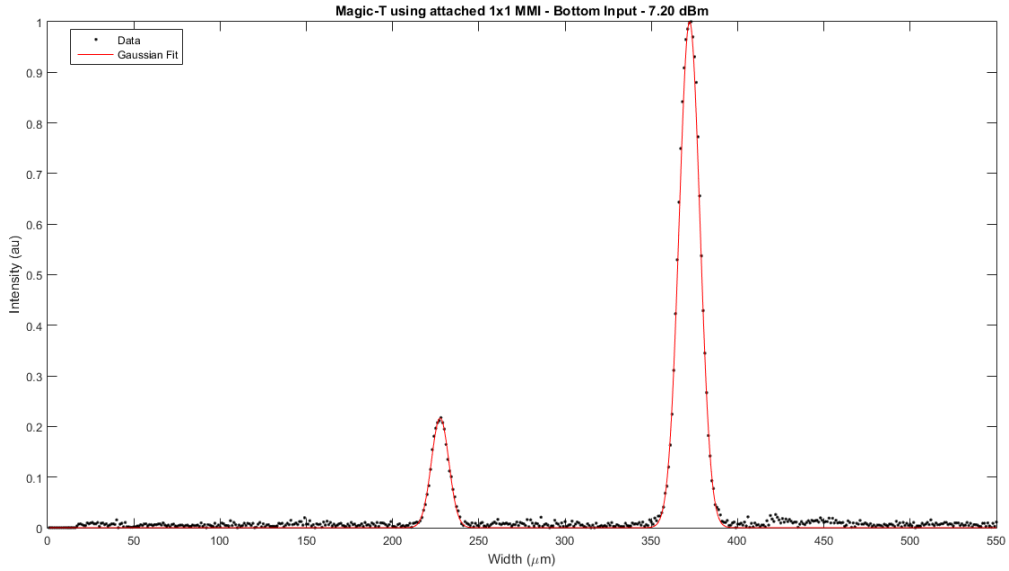

Figure 5.41: Magic-T using attached 1x1 MMI device - Bottom Input - +7.2 dBm

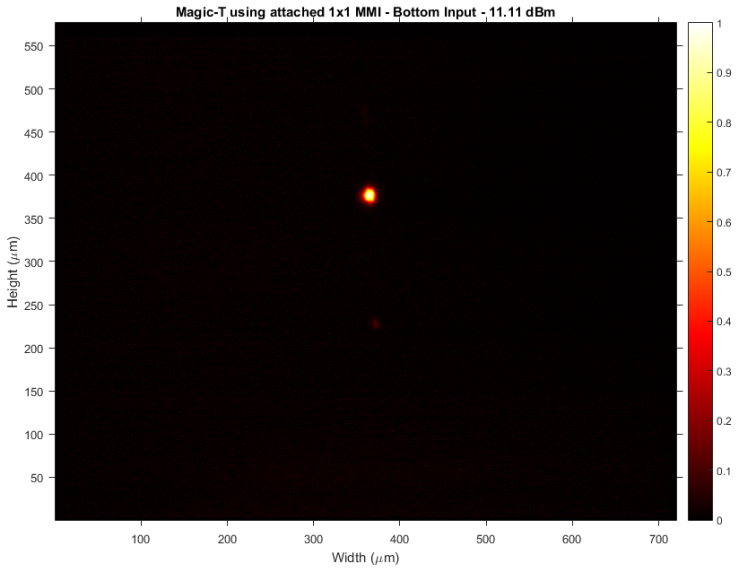

Figure 5.42: Magic-T using attached 1x1 MMI device - Bottom Input - +11.1 dBm

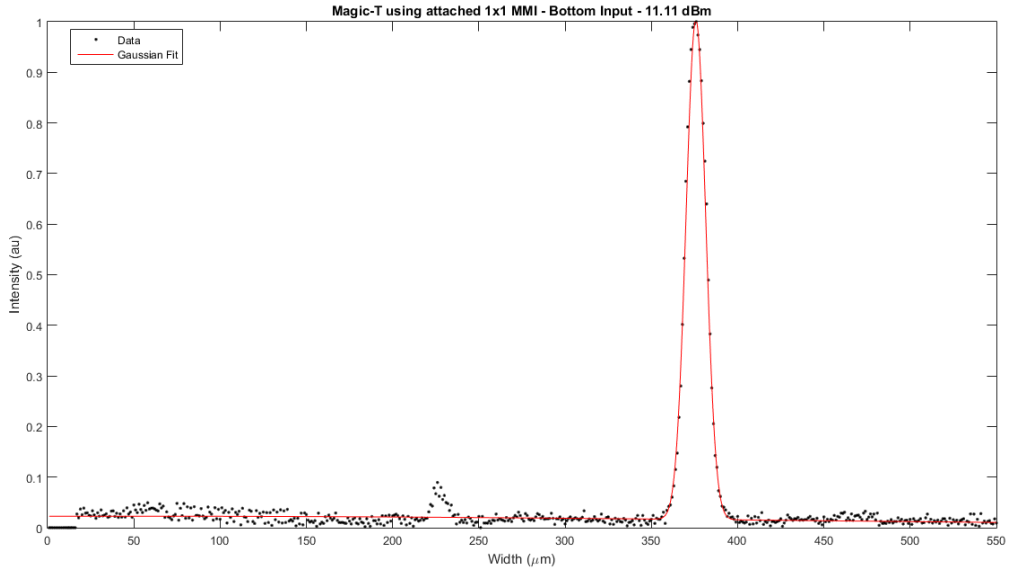

Figure 5.43: Magic-T using attached 1x1 MMI device - Bottom Input - +11.1 dBm

Beam	FWHM (μm)	Peak Position (μm)	Height (au)	Area (au)
1	11.8685	226.5237	0.2168	2.7388
2	14.1939	371.1267	1	15.1089

Relative Power Loss		
Beams	**%**	**dB**
1-2	81.9	-7.42
Total vs 1	84.7	8.15
Total vs 2	15.3	0.72

Table 5.17: Magic-T using attached 1x1 MMI device - Bottom Input - +7.2 dBm

Beam	FWHM (μm)	Peak Position (μm)	Height (au)	Area (au)
1	13.5818	374.7786	1	14.5047

Table 5.18: Magic-T using attached 1x1 MMI device - Bottom Input - +11.1 dBm

Once again, the tests achieved the expected results. With +7.2 dBm, the outputs' ports are distinct and the behavior follows the same path as in with both inputs connected to the splitter. With the higher input power, the efficiency drastically improves and the sub port is not even visible, being the sum output the only one available to get values from.

These last tests prove that the circuit with the attached MMI devices to the Magic-T is more efficient than the one with the detached MMI components. The fact that they are attached minimizes the power dispersion losses and helps the laser to navigate better the waveguides entering and exiting the Magic-T.

5.2.6 Magic-T using 8x8 MMI

This circuit was tested, even if it was never meant to work. Issues with the design of the circuit and the complexity of its components do not allow the capture of valid data since the outputs kept changing their intensity profiles. The Magic-T using an 8x8 MMI device can be seen below (Figure 5.44):

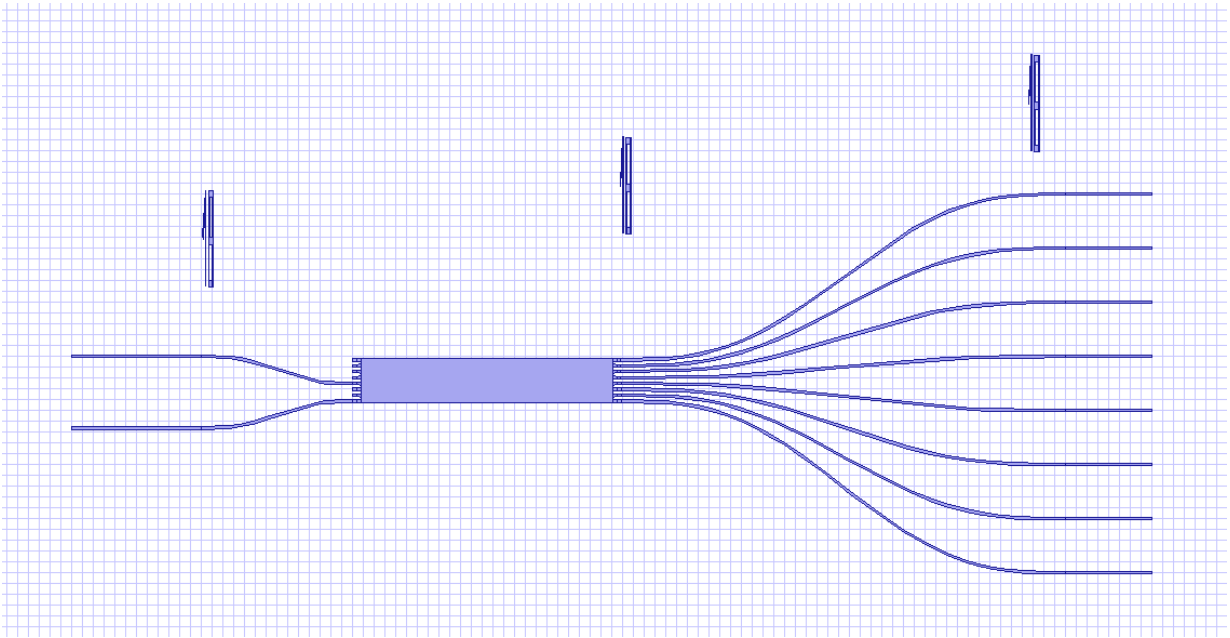

Figure 5.44: Magic-T using 8x8 MMI device

Nevertheless, Figures 5.45 to 5.48 and Tables 5.19 and 5.20 show what was able to be obtained from the circuit with an input power of +7.2 dBm.

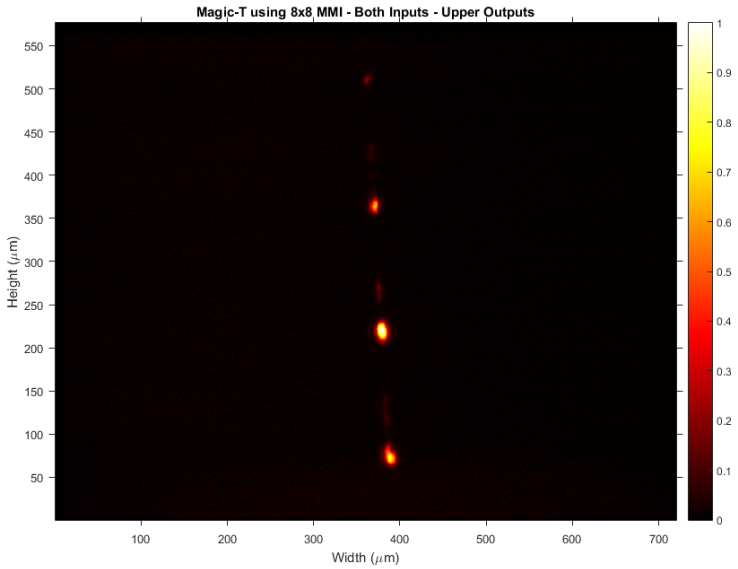

Figure 5.45: Magic-T using 8x8 MMI device - Upper Outputs

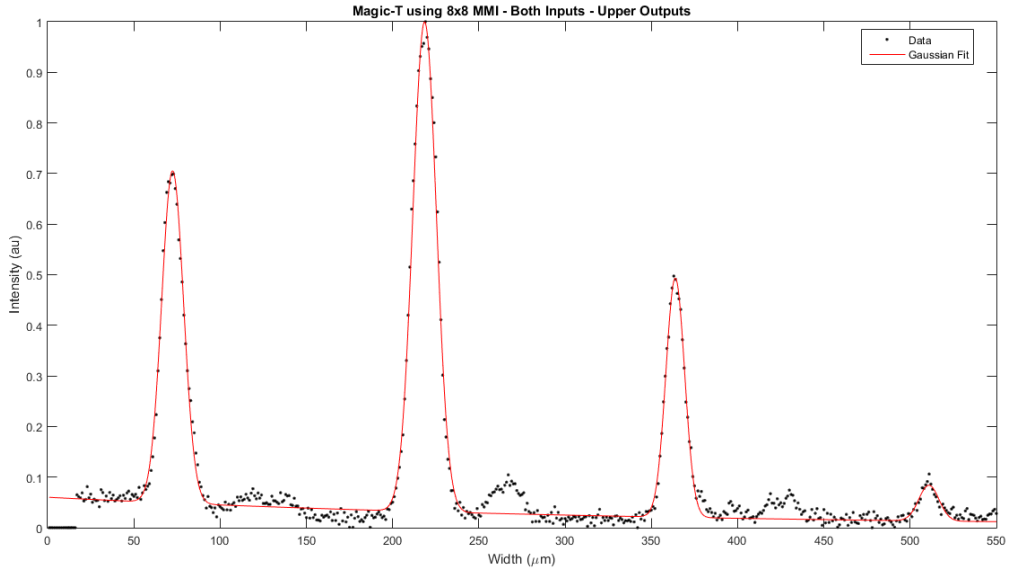

Figure 5.46: Magic-T using 8x8 MMI device - Upper Outputs

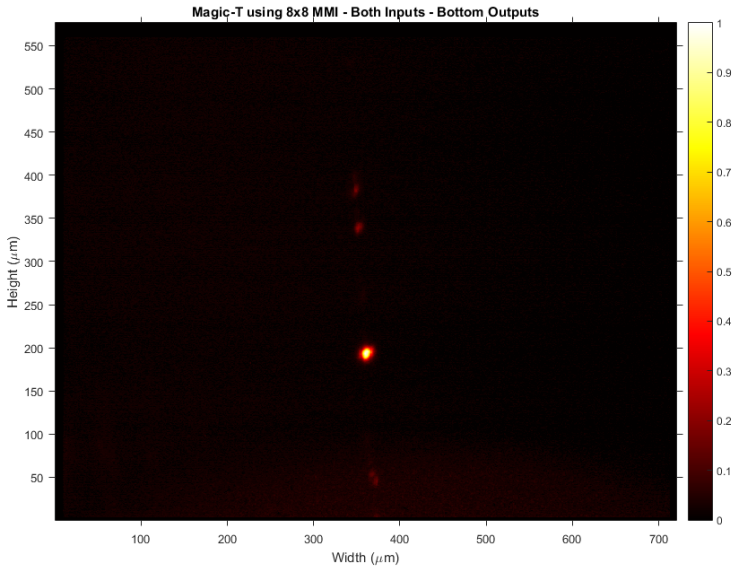

Figure 5.47: Magic-T using 8x8 MMI device - Bottom Outputs

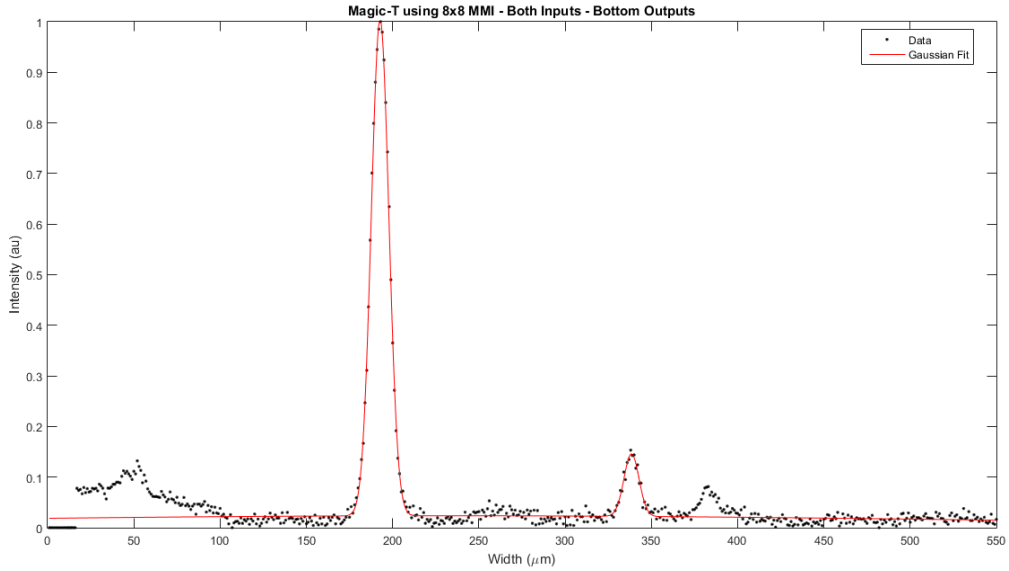

Figure 5.48: Magic-T using 8x8 MMI device - Bottom Outputs

Beam	FWHM (μm)	Peak Position (μm)	Height (au)	Area (au)
1	15.7510	71.4422	0.7053	11.8255
2	16.4997	217.5314	0.9997	17.5586
3	13.2003	362.8434	0.4934	6.9334
4	15.6702	509.8380	0.0840	1.4007
	Relative Power Loss			
	Beams	**%**	**dB**	
	1-4	88.2	9.28	
	2-4	92.0	10.97	
	3-4	79.8	6.95	
	1-3	41.4	2.32	
	2-3	60.5	4.03	
	1-2	32.7	-1.72	

Table 5.19: Magic-T using 8x8 MMI device - Upper Outputs

Beam	FWHM (μm)	Peak Position (μm)	Height (au)	Area (au)
1	12.1986	191.7228	1	13.0293
2	11.6555	337.4583	0.1458	1.8094
	Relative Power Loss			
	Beams	**%**	**dB**	
	1-2	86.1	8.57	

Table 5.20: Magic-T using 8x8 MMI device - Bottom Outputs

5.3 Four-Input Circuits Testing Process

The four-input circuits implemented the HWT with the Magic-T and 1x1 MMI devices (example in Figure 5.49). However, the distance between waveguides for these circuits was not the $125\mu m$ but a bit more. Therefore, the fiber array could not be aligned with any of these circuits.

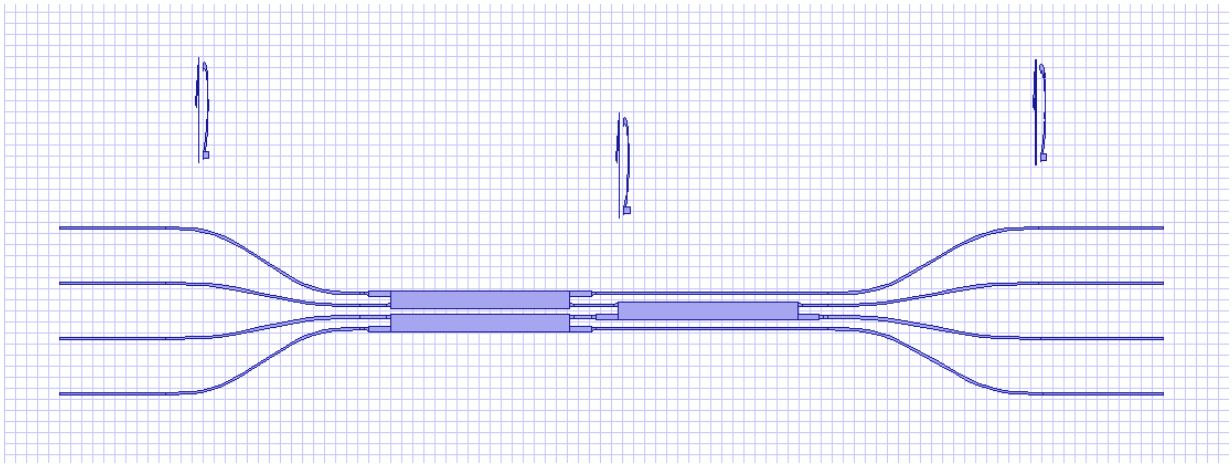

Figure 5.49: HT with Magic-T using attached 1x1 MMI devices

The reason behind the larger distances than what was designed has to do with the photolithography process. Since the circuits are more complex, i.e., more components and more waveguides, the radiation printing might not be as effective as it should. The angle of incidence of the UV pulsed laser could also be a major reason of this issue since a small deviation from the supposed 90° affects more a four-input circuit than a two or one-input one.

Attempts to align the fiber array with the existing four circuits of this type ended up failing, and the other samples have these circuits in worse conditions (dust, holes, access waveguides poorly printed).

Chapter 6

Conclusions and Future Work

This dissertation main objective was to test optical compression circuits based on HWT and MMI mechanisms, which were going to be printed through a photolithography process. Before the experimental work began, an in-depth study of the most significant concepts had to be performed.

Firstly, an overview of the theory behind the HT was explored. This helped to understand better how image processing and compression mathematically work, but also to develop some knowledge regarding the transform's history. Then, an analysis of Soldano and Pennings [3] was needed to understand the methodology behind the types of MMI mechanisms. With all of this knowledge acquired, the laboratory work started.

The photolithography process demanded a remarkably well-adjusted setup and an overall understanding of each material's objectives and specifications. Some mid-printing tests had to be performed to understand better how the UV pulsed laser related with time, energy and temperature. The resulting four samples, each printed with circuits based on the concepts mentioned earlier, passed through a visual inspection using a microscope. This was required to understand which circuits were in better conditions to be tested.

Finally, the circuits characterization was the last step. From the several types of circuits, the two-input circuits were tested in an experimental setup similar to the one used for one-input circuits, with the addition of a power splitter and the use of a handmade fiber array. Therefore, some issues witnessed in the circuit's behavior might originate from some small phase deviation between the fibers in the array. The software used a CCD camera to capture essential parameters from the output's beams, such as intensity profiles, beam widths and more.

Using MATLAB to fit the results into a Gaussian approximation, the mathematical analysis was complete. The three circuits successfully tested contained solely a Magic-T

or MMI devices attached or detached from a Magic-T. Some important conclusions were made:

- the Magic-T has the sum and sub mechanisms well-implemented, as it can be proved by the tests performed on the first circuit;
- the MMI components bring more efficiency to the circuits due to their interference mechanisms;
- the attached MMI devices are a more efficient solution than the detached ones due to the minimized losses and better noise cancellation;
- a fourth circuit containing an 8x8 MMI was not able to be tested due to some issues regarding the sophisticated design of the components.

Regarding future work inside this project, there are some clear paths in need of following. The four-input circuits need to be tested, and it is a definite next step, as well as a very well-prepared experimental approach to deal with phase deviation between inputs.

Bibliography

[1] Piotr Porwik and Agnieszka Lisowska. "The Haar-wavelet transform in digital image processing: its status and achievements". In: *Machine graphics and vision* 13.1/2 (2004), pp. 79–98.

[2] Giorgia Parca, Pedro Teixeira, and Antonio Teixeira. "All-optical image processing and compression based on Haar wavelet transform". In: *Applied optics* 52.12 (2013), pp. 2932–2939.

[3] Lucas B Soldano and Erik CM Pennings. "Optical multi-mode interference devices based on self-imaging: principles and applications". In: *Journal of lightwave technology* 13.4 (1995), pp. 615–627.

[4] RAS Ferreira, PS André, and LD Carlos. "Organic–inorganic hybrid materials towards passive and active architectures for the next generation of optical networks". In: *Optical Materials* 32.11 (2010), pp. 1397–1409.

[5] Carlos MS Vicente et al. "Thin film optimization design of organic–inorganic hybrids for waveguide high-rejection optical filters". In: *physica status solidi (RRL)–Rapid Research Letters* 5.8 (2011), pp. 280–282.

[6] Carlos Miguel Santos Vicente. "Híbridos orgânicos-inorgânicos para aplicações de baixo custo em óptica integrada". In: (2012).

[7] Giorgia Parca et al. "Optical Haar transform for 2D processing and compression". In: *Transparent Optical Networks (ICTON), 2013 15th International Conference on*. IEEE. 2013, pp. 1–4.

[8] L Almeida et al. "All-Optical image processing based on integrated optics". In: *Transparent Optical Networks (ICTON), 2014 16th International Conference on*. IEEE. 2014, pp. 1–5.

[9] Giorgia Parca, Pedro Teixeira, and Antonio Teixeira. "3D interferometric integrated passive scheme for all optical transform". In: *Transparent Optical Networks (ICTON), 2012 14th International Conference on*. IEEE. 2012, pp. 1–4.

[10] Giorgia Parca, Pedro Teixeira, and António Teixeira. "All-Optical Integrated System for 2D Data Wavelet Transform and Compression". In: *Electrónica e Telecomunicações* 5.4 (2012), pp. 446–449.

[11] João Diogo Victor Fernandes. "Haar transform based on a 2 x 2 multimode interferometer". MA thesis. Universidade de Aveiro, 2016.

[12] Tetsuya Mizumoto and Yoshiyuki Naito. "Dependence of the output phase difference on the asymmetry of 3-dB directional couplers". In: *Journal of Lightwave Technology* 8.10 (1990), pp. 1571–1576.

[13] Trung-Thanh Le. "The Design of Optical Signal Transforms Basedon Planar Waveguides on a Silicon on Insulator Platform". In: *International Journal of Engineering and Technology* 2.3 (2010), p. 245.

[14] *List of Equipment of the Optical Communications Group*. Instituto de Telecomunicações - Pólo de Aveiro. Aug. 2017.

[15] Daniela C Oliveira et al. "Photopatternable di-ureasil- zirconium oxocluster organic-inorganic hybrids as cost effective integrated optical substrates". In: *Chemistry of Materials* 20.11 (2008), pp. 3696–3705.

[16] Vasco R Fernandes et al. "Determination of refractive index contrast and surface contraction in waveguide channels using multiobjective genetic algorithm applied to spectroscopic ellipsometry". In: *Journal of Lightwave Technology* 29.19 (2011), pp. 2971–2978.

[17] *Area under Gaussian peak by easy measurements*. 2010 (accessed June 6, 2018). URL: `https://www.physicsforums.com/threads/area-under-gaussian-peak-by-easy-measurements.419285/`.

[18] Rute AS Ferreira et al. "Photonic-on-a-chip: a thermal actuated Mach-Zehnder interferometer and a molecular thermometer based on a single di-ureasil organic-inorganic hybrid". In: *Laser & Photonics Reviews* 7.6 (2013), pp. 1027–1035.